

A New Monte-Carlo Model for the Space Environment

Daniel Jang ^{*}, Davide Gusmini [†] Peng Mun Siew [‡]
Massachusetts Institute of Technology, Cambridge, MA 02139

Andrea D'Ambrosio [§]
University of Arizona, Tucson, AZ 85721

Simone Servadio [¶]
Iowa State University, IA 50011

Pablo Machuca ^{||}
San Diego State University, CA 92182

Richard Linares ^{**}
Massachusetts Institute of Technology, Cambridge, MA 02139

This paper introduces a novel Monte Carlo (MC) method to simulate the evolution of the low-earth orbit environment, enhancing the MIT Orbital Capacity Analysis Tool (MOCAT). In recent decades, numerous space environment models have been developed by government agencies and research groups to understand and predict the dynamics of space debris. Our MC approach advances this by simulating the trajectories of space objects and modeling their interactions, such as collisions and explosions. This aids in analyzing the trends of space-object and debris populations. A key innovation of our method is the computational efficiency in orbit propagation, which is crucial for handling potentially large numbers of objects over centuries. We present validation results against the IADC (Inter-Agency Space Debris Coordination Committee) study and explore various scenarios, including ones without future launches and those involving the launch of proposed megaconstellations with over 80,000 active payloads. With the improvement in computational efficiencies provided by this work, we can run these new scenarios that predict millions of trackable objects over a 200-year period. The previous state-of-the-art was 400,000 objects over the same period of time. Notably, while fewer megaconstellations are planned for altitudes above 800 km, even minimal failures in

^{*} *Corresponding Author.* Ph.D. Candidate, Department of Aeronautics and Astronautics, Massachusetts Institute of Technology, MA 02139, USA. email: djang@mit.edu

[†] Visiting Graduate student, Department of Aeronautics and Astronautics, Massachusetts Institute of Technology, MA 02139. email: gusmini.dav@gmail.com

[‡] Research Scientist, Department of Aeronautics and Astronautics, Massachusetts Institute of Technology, MA 02139, USA. email: siewpm@mit.edu

[§] Postdoctoral Associate, System & Industrial Engineering Department, University of Arizona, Tucson, AZ 85721, USA; email: dambrosio@arizona.edu

[¶] Assistant Professor, Department of Aerospace Engineering, Iowa State University, IA 50011, USA. email: servadio@iastate.edu

^{||} Visiting Professor, Department of Aerospace Engineering, San Diego State University, CA 92182, USA. email: pmachuca@sdsu.edu

^{**} Rockwell International Career Development Professor, Associate Professor of Aeronautics and Astronautics, Department of Aeronautics and Astronautics, Massachusetts Institute of Technology, Cambridge, MA 02139, USA. email: linaresr@mit.edu

post-mission disposal or collision avoidance maneuvers can significantly impact orbital debris accumulation.

Nomenclature

AMR	Area to Mass Ratio
CAM	Collision Avoidance Maneuver
CARA	Conjunction Assessment Risk Analysis
ECI	Earth Centered Inertial Coordinate System
ESA	European Space Agency
FCC	Federal Communications Commission
FD	Fragmentation Debris
GEO	Geosynchronous Orbit
ISS	International Space Station
ITU	International Telecommunication Union
LEO	Low Earth Orbit (LEO)
LNT	Lethal Non-Trackable
MASTER	ESA's Meteoroid And Space debris Terrestrial Environment Reference
MC	Monte Carlo
MITRI	MIT Risk Index
MOCAT	MIT Orbital Capacity Analysis Tool
MRO	Mission Related Objects
NASA	National Aeronautics and Space Administration
NFL	No Future Launch
PL	Payload

RB	Rocket Body
SGP4	Simplified General Perturbations Satellite Orbit Model 4
SSEM	Source Sink Evolutionary Model
TLE	Two-Line Element
α	Collision avoidance failure rate between active and non-active objects
α_a	Collision avoidance failure rate between active objects
Δt	Simulation time step
Ω	Right Ascension of the Ascending Node (RAAN)
ω	Argument of perigee
ρ	Atmospheric density
σ	Cross sectional area
\tilde{E}_p	Specific energy in a collision
A	Area
a	Semi-major axis
A_p	Geomagnetic planetary index
B^*	B^* or Bstar parameter
C_D	Drag coefficient
dU	Inverse of the volume of cube
e	Orbit eccentricity
f	True anomaly
i	Inclination
J_2	Earth's oblateness
L_C	Characteristic length
M	Mean anomaly

m	Mass
P_C	Probability of collision
P_{PMD}	Probability of succesful PMD
PDF	Probability density function
r	Radius of object
R_E	Earth radius
$r_{x,y,z}$	ECI position vector components
s_i	Spatial density of objects of type i
t	Time
v_c	Collision velocity
$v_{x,y,z}$	ECI velocity vector components
CDM	Conjunction data message
T	Temperature

I. Introduction

Space debris has emerged as a critical environmental and political issue due to the substantial increase in space objects, especially in the Low Earth Orbit (LEO). Several factors contribute to this recent increase in the number of objects, including cost-efficient launches, increased commercial activity, and recent debris-creating events in space, such as explosions and collisions, including anti-satellite weapon tests. In particular, recent advances in orbital launch technologies and the growth of commercial launch providers have made LEO launches much cheaper and more reliable, leading to a new space age. Until recently, the increase in object number in space was around 300 objects per year; however, increased launch cadence and the rise of large LEO constellations have led to a marked increase in LEO population. For example, from 2019 to 2023, SpaceX alone has launched more than 5,500 satellites [1]. The US Federal Communications Commission (FCC) and the United Nations International Telecommunication Union (ITU) filings show that companies or governments are asking for approvals for constellations that are greater than the current number of objects in space.

As debris from fragmentation events create more debris, it may be possible to create a cascading effect of chain reactions, which is a phenomenon known as Kessler syndrome [2, 3], which may render certain altitudes unusable and

threaten the sustainability of space operations. The primary natural sink to remove space debris from LEO is the upper atmosphere's low density; there is a limit to how much collision can be tolerated in LEO, which is highly dependent on the orbital altitude.

Recent advances in technologies and policies addressing the space debris problem encompass several key areas. Active Debris Removal (ADR) technologies are being developed, including systems such as harpoons, nets, robotic arms, and space tugs, to capture, deorbit, or mitigate the effects of space debris [4–8].

Addressing the space debris problem requires global collaboration, responsible space practices, effective debris mitigation strategies, and the advancement of technologies for active debris removal and improved space situational awareness (SSA). In particular, space debris models guide policies and strategies for space traffic management, debris mitigation, and spacecraft design to ensure the sustainability of space activities. Over the years, studies have shown the dangers of this increased population, and policies and metrics have been proposed to counteract the increased risk in the space environment [9–15]. Recently, debris mitigation policies such as the '5-year rule' [16] and resolutions to limit debris-causing antisatellite tests have come from the United Nations and the commercial space industry [17, 18].

To understand the complex dynamics of space debris, sophisticated modeling approaches have been developed in the literature. Kessler's paper in 1978 originally described the potential for runaway growth of orbital debris due to debris that causes more debris through collisions, which could lead to an unusable orbital environment [2]. Since then, several analytical methods have been proposed in the literature to better quantify this risk [8, 19, 20], which can be divided into a few categories. There are largely two methods to model the evolution of the LEO orbital population and collision risk: statistical sampling methods such as Monte Carlo methods and source-sink models, also known as particle-in-box models. There are also heuristic metrics to quantify the risk per object for any particular composition of the LEO environment, which is described below.

Space agencies and organizations often use heuristic methods and metrics for decision making when planning missions or strategies to ensure space sustainability. These indicators are metrics used to assess the potential danger posed by an orbital object and help prioritize the management and mitigation of space debris by evaluating the risk associated with individual debris objects. The Criticality of Spacecraft Index (CSI) ranks the environmental criticality of abandoned objects in LEO [21]. It takes into account the physical characteristics of a given object, its orbit, and the environment in which it is located. Environmental Consequences of Orbital Breakups (ECOB) is based on the evaluation of the consequences of the fragmentation of the studied object in terms of the increase in the collision probability for operational satellites. This index considers the likelihood and consequence of fragmentation and end-of-life mitigation strategies [19].

In [22] numerous international space organizations contributed lists of the top 50 concerning objects, which were compared using multiple algorithms to create a ranked composite list. Factors such as mass, encounter rates, orbital lifetime, and proximity to operational satellites were shown to be crucial. Similarly, the MIT Risk Index (MITRI) is

an index to help identify the most dangerous debris that can be removed considering the requirements of the chaser spacecraft and the constraints of the mission [8]. The index considers the proximity of the debris to highly populated regions, its persistence in orbit, its likelihood to collide, and the estimated number and mass of debris it can generate.

The source-sink evolutionary models describe the interactions between objects populations with ordinary differential equations, first used to describe predator prey interaction between fish population [23] and the chemical reactions [24]. For example, if all space objects of interest are categorized as payloads, derelict satellites, or debris, three ordinary differential equations can describe the interaction between these populations. Average values are often used to describe the population's characteristics, such as a population's size, velocity, rate of launch, and failure rate. This simplification eliminates the need for computationally expensive propagation of individual object states to estimate a future debris environment. Gross populations are propagated forward according to the governing differential equations, allowing fast solutions even far into the future. Exploring a wide set of initial conditions and parameters is much more approachable using such methods. These methods are also usually deterministic in that, given a set of input variables, a consistent output can be expected as the variables interact in a formalized manner.

Kessler and Cour-Palais first described the feedback runaway phenomenon and identified the risk of an exponential increase in the number of space debris [2], and since then a few evolutionary models have been proposed in the literature. Talent introduces the particles-in-box (PIB) model in which a population within an orbital shell is assumed to have some average characteristic and interactions [25]. Fast Debris Evolution (FADE) used simplified first-order differential equations to describe the population interaction [4]. JASON describes a three-population model for one shell and a given launch cadence [26]. Many models have expanded the evolutionary model to analyze multiple shells, optimal control schemes, and economic equilibrium for maximum policy intake. The MIT Orbital Capacity Tool Source-Sink Evolutionary Model (MOCAT-SSEM) is able to create a flexible and modular multifidelity model to rapidly model the evolution of the LEO population [27–29]. The low computational cost demonstrates the ability to optimize user-defined cost functions for policy-making and governance, and calculate the risk-based space environment capacity [30] and has been expanded to include orbit-raising dynamics [28], as well as calculation of risk-based orbital capacity [29].

Statistical sampling methods propagate every object's orbital states with high fidelity propagators to estimate the future space environment at some small time steps, much like a particle filter. Several such sampling-based models have been developed by space agencies and private entities as a result of the large-scale development and support required. Examples include NASA's Orbital Debris Engineering Model (ORDEM) and LEO to Geosynchronous Orbit Debris model (LEGEND)[31], European Space Agency's Orbital Debris Evolutionary Model (ODEM), Chinese Academy of Sciences' SOLEM (Space Objects Long-term Evolution Model), University of Southampton and United Kingdom Space Agency's Debris Analysis and Monitoring Architecture for the Geosynchronous Environment (DAMAGE)[32, 33], MEDEE model from Centre National d'Etudes Spatiales [34], DELTA model from European Space Agency [35], LUCA model from Technische University at Braunschweig [36], NEODEEM model from Kyushu University and the Japan

Aerospace Exploration Agency, IMPACT [37], and others [38–40]. A probabilistic debris environment propagator has been explored in [41] where objects are classified as either intact objects or fragments and accounts only for collisions between the two classes. This simplification allows for computational efficiency, and validation work is on-going.

For each of these models, the debris population and densities are outputted given some input initial conditions and assumptions. However, computing a debris environment with different sets of assumptions requires high computational cost, as each object must be propagated. Sampling over a distribution of uncertainties in states and parameters would require an exponential number of propagations. The high cost is due to the small time steps required to accurately model a collision and semi-analytical propagators requiring high compute cost to propagate far into the future. For each collision or fragmentation event, a breakup model, such as the NASA Standard Breakup Model (SBM) is used to model the debris cloud generation. Although the outputted debris distribution for some assumed initial conditions and future traffic models exists, all of these models are closed-source and inputting arbitrary assumptions is difficult if not impossible.

The establishment of a common, validated, and open-source model for space debris is imperative for several reasons. Firstly, such a model ensures standardization and consistency between stakeholders, creating a shared language and methodology for analyzing space debris. This framework facilitates effective communication and information sharing among governments, space agencies, researchers, and industry players. In addition, a validated model improves accuracy in assessing collision risks and predicting debris behavior, crucial for ensuring the safety of spacecraft, satellites, and astronauts in orbit.

In this paper, an MC method is developed and described to simulate the evolution of the LEO environment called MOCAT-MC. It is a full-scale three-dimensional debris evolutionary model that propagates individual objects and models the interactions between objects at each time step, with the aim of assessing the LEO population. The development of MOCAT-MC will provide an open-source validated tool that can be accessed and used by the space-debris community.

One of the drawbacks of MC methods is the high computational time required to run the simulations, and particular attention is given to the computational speed of all sub-modules of MOCAT-MC. Several phenomena are considered, such as the atmospheric model and the propagator, active satellite station-keeping, new launches, reentry, post-mission disposal (PMD), explosions, and collisions. Active payloads maintain orbital altitude to counteract the effects of atmospheric drag, while new launches are introduced into the simulation. Certain payloads are deliberately deorbited through PMD and removed from the simulation due to atmospheric reentry. A successful PMD is assumed to include the entire deorbit cycle from mission orbit to atmospheric reentry. However, some satellites may fail to execute PMD with some given probability, transitioning into an inactive state, and remaining in its orbit as a derelict object.

Explosions are simulated with a predefined probability, leading to the creation of smaller debris as described by the NASA Standard Breakup Model [42]. The characteristics of these newly generated objects, such as quantity, direction, and size, are determined by the model. The Cube method is used to determine collisions between two objects [43, 44],

and results in the generation of numerous debris objects within the simulation as dictated by the NASA SBM.

This work makes several contributions to the literature, including:

- First open-source MC-based evolutionary orbital population model with modular sub-components to allow for numerous propagations, and collision detection algorithms.
- Simulation of tens of millions of orbital objects centuries into the future using a single processing thread.
- Demonstration that analytical propagation can be used to scale MC simulations.
- Output of collision statistics and collision avoidance burden.
- First analysis of future constellation traffic as filed with ITU and FCC, reaching 82,000 operational satellites in LEO from the megaconstellations alone.

MOCAT was developed in MATLAB and is open-source [45]. The paper is organized as follows. The MOCAT-MC model is explained in Section II. Section III shows the MOCAT-MC validation exercise against existing scenarios and results in the literature, and Section IV shows the result from the no future launch scenario, as well as the FCC/ITU filed megaconstellations. Section V summarizes the contribution of this paper.

II. Methodology

MOCAT-MC has multiple submodules, which is shown in the functional diagram in Figure 1 as described in [8].

The description of each of these components is described in this section.

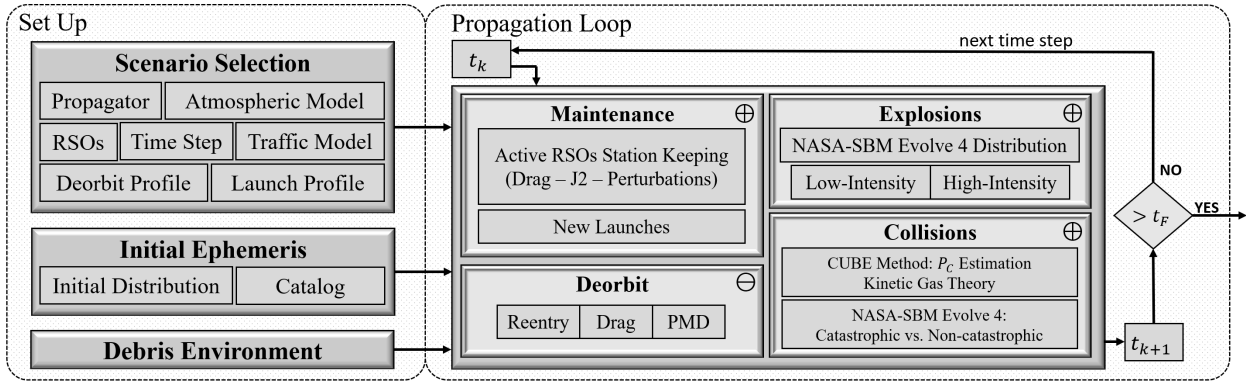


Fig. 1 Schematic of the Monte Carlo tool MOCAT-MC

A. Analytical Propagator

The SGP4 propagation method [46] is a common approach for analytically propagating orbital states. However, other semi-analytical and analytical propagators could represent a better choice in terms of a compromise between fidelity and computational time. Therefore, in MOCAT-MC, an analytical approximation of the solution for the motion of the LEO objects is used, with perturbations from atmospheric drag and J_2 . The initial ephemeris is also loaded,

which can be seeded with an existing catalog such as the Two Line Element (TLE) catalog provided publicly by the 18th Space Defense Squadron*.

An averaging perturbation technique has been employed to obtain the variational equations for the orbital elements with the combined effect of J_2 and drag as described in [47]. Implementation of other propagators such as the Draper Semi-analytical Satellite Theory (DSST) [48] and SGP4 [46] is reserved for future work, though these will require a higher computational burden compared to the analytical propagator. The propagator is based on two assumptions: the atmospheric density is constant and the orbit eccentricity is small. However, in the implementation of the analytical propagator, a time-varying atmospheric model is modeled with a piecewise continuous formulation with a mean solar activity [49] rather than a static atmospheric density. This allows for the effects of geomagnetic storms and solar cycles to be modeled, which can strongly affect the atmospheric density.

Let us define

$$\alpha_0 = \frac{\bar{e}_0}{\sqrt{\bar{a}_0}}, \quad \beta_0 = \frac{\sqrt{3}}{2} \bar{e}_0, \quad \bar{n}_0 = \sqrt{\frac{\mu}{a_0^3}}; \quad (1)$$

and indicate with $c = \cos \bar{i}$ the cosine of the inclination. The resulting set of equations used for the propagation is

$$\begin{aligned} \bar{a} &= \frac{\bar{a}_0}{\beta_0^2} \tan^2 [\arctan(\beta_0) - \beta_0 \bar{n}_0 \bar{a}_0 C_0 (t - t_0)] \\ \bar{e} &= \frac{2}{\sqrt{3}} \tan [\arctan(\beta_0) - \beta_0 \bar{n}_0 \bar{a}_0 C_0 (t - t_0)] \\ \bar{M} - \bar{M}_0 &= \frac{1}{8} \frac{1}{C_0} \left[\frac{4}{\tau} + 3\alpha_0^2 \ln \left(\frac{\tau}{\bar{a}_0} \right) \right] \Bigg|_{\tau=\bar{a}_0}^{\tau=\bar{a}} + \frac{3k_2 (3c^2 - 1)}{16\mu} \frac{1}{C_0} \left[\frac{3\alpha_0^2}{2} \frac{1}{\tau^2} + \frac{4}{3\tau^3} \right] \Bigg|_{\tau=\bar{a}_0}^{\tau=\bar{a}} \\ \bar{\omega} - \bar{\omega}_0 &= \frac{3k_2 (5c^2 - 1)}{16\mu} \frac{1}{C_0} \left[\frac{5\alpha_0^2}{2} \frac{1}{\tau^2} + \frac{4}{3\tau^3} \right] \Bigg|_{\tau=\bar{a}_0}^{\tau=\bar{a}} \\ \bar{\Omega} - \bar{\Omega}_0 &= -\frac{3k_2 c}{8\mu} \frac{1}{C_0} \left[\frac{5\alpha_0^2}{2} \frac{1}{\tau^2} + \frac{4}{3\tau^3} \right] \Bigg|_{\tau=\bar{a}_0}^{\tau=\bar{a}} \end{aligned} \quad (2)$$

where $[\bar{a}, \bar{e}, \bar{i}, \bar{\Omega}, \bar{\omega}, \bar{M}]^T$ represents the state vector at the current time t : semi-major axis, eccentricity, inclination, right ascension of the ascending node, argument of periapsis, and mean anomaly, respectively. The subscript 0 denotes the state variables at the initial time of propagation t_0 , and $k_2 = \mu J_2 R_E^2 / 2$ and $C_0 = \frac{1}{2} C_D \frac{A}{m} \rho_0$, with μ and R_E representing the gravitational parameter and radius of the Earth, respectively, ρ the atmospheric density, and C_D , A , and m representing the drag coefficient, area, and mass, respectively.

Before introducing the time-varying model of atmospheric density in the next section, a static exponential atmospheric model is used to test the validity of the analytical equations of motion in Eq. (2) compared to a numerical propagator

*<https://www.space-track.org>

that includes the drag and J_2 effects. For a given initial population of objects between 200 and 2,000 km altitudes and a propagation duration of one year, several relevant metrics are used for validation purposes: number of objects still in orbit depending on initial altitude h_0 ; reduction in the semi-major axis depending on h_0 and decay in right ascension depending on h_0 ; and finally the time to decay depending on h_0 . Figures 2 to 5 show the validation results.

Figure 2, for instance, illustrates the number of objects as a function of altitude, in the initial population and after the one-year propagation. It can be observed that the distributions of objects obtained by the analytical propagator and by the numerical propagator show strong agreement. The analytical propagator can effectively approximate the number of objects expected as a function of altitude. From Figure 3, it is shown that the analytical propagator typically underestimates the decay in the semi-major axis due to drag, but the overall distribution of semi-major decay as a function of altitude resembles that of the numerical propagator. On the contrary, in Figure 4, it is observed that the decrease in right ascension is usually overestimated by the analytical propagator, but the overall distribution of the decrease in right ascension as a function of altitude is also similar to that displayed by the numerical propagator. Lastly, and related to the results in Figure 3, it is observed in Figure 5 that the time to decay is usually overestimated by the analytical propagator, but the distribution of time to decay as a function of altitude produced by the analytical propagation also resembles that produced by the numerical propagator. Although certain quantitative discrepancies appear between the analytical and numerical propagators, the analytical solution is able to capture the overall effects of drag and J_2 as a function of time, while achieving orders of magnitude shorter computational times: which is particularly meaningful when propagating tens of thousands to millions of orbital objects.

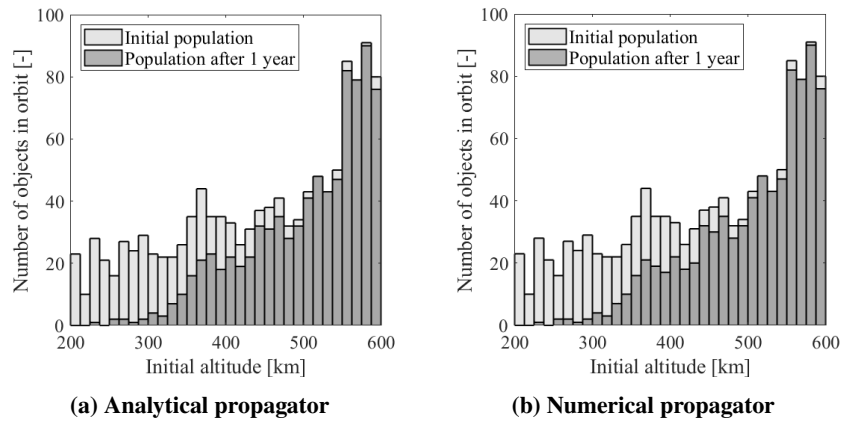


Fig. 2 Number of objects in orbit depending on initial altitude

B. Initial Population and Data Sources

Simulations that have a basis in today's orbital environment require some data to seed the initial population. A range of orbital parameters can be provided to the simulation, which can be sampled to seed the initial orbital distribution. Each object can have a unique lifetime, station-keeping methods, failure rate, size, etc. to characterize its behavior and

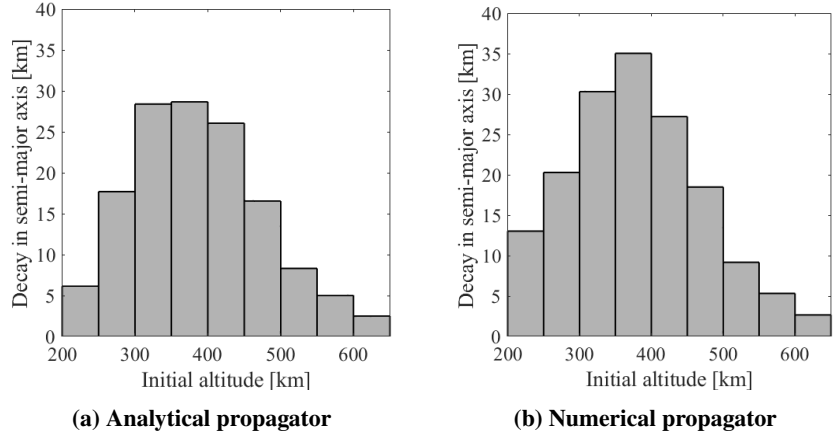


Fig. 3 Decay in semi-major axis depending on initial altitude

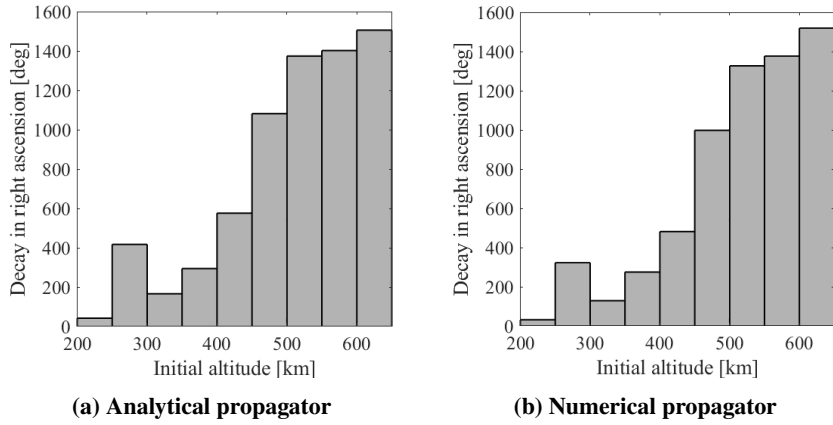


Fig. 4 Decay in right ascension depending on initial altitude

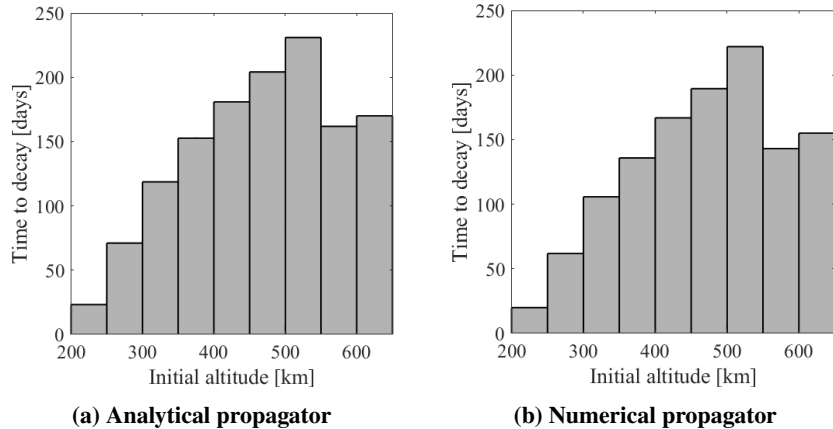


Fig. 5 Time to decay depending on initial altitude

potential interaction with other objects. The initial debris environment is determined. Depending on the analysis, the size, number, and orbital parameters of these objects can be set. The minimum size debris to be considered in the model will also be an input parameter, which will affect the number of objects in the simulation. The probability distribution

function (PDF) of the debris population parameters can be supplied from LEO debris models such as ESA’s MASTER model [50] and the current space catalog.

Two Line Element sets (TLEs) are used to identify objects that are currently in orbit around Earth. The model considers a total of around 24,000 space objects obtained from Space-Track (as of September 2022)*. In order to have a complete dataset, some other information such as mass, diameter, status, object-class, and launch date need to be gathered. The physical characteristics, the date of launch, and the object-class are retrieved through DISCOS† developed by the European Space Agency. For up-to-date active/inactive status of payloads Celestrak‡ is used. This may be important, as active payloads are able to perform station keeping and collision avoidance maneuvers and may attempt to dispose after their mission is over. After processing the data, MIT’s catalog with an epoch of January 1 2022 consists of 21,014 TLEs, out of which 10,869 are debris, 7,015 payloads of which 5,129 active and 1,886 inactive, 1,421 rocket bodies, and the remaining 1,709 Mission Related Objects (MRO).

Table 1 Definition of parameters for each orbital object in MOCAT-MC

Column	1 - 6	7	8	9	10	11	12
Description	$\bar{a}, \bar{e}, \bar{i}, \bar{\Omega}, \bar{\omega}, \bar{M}$	B^*	Mass	Radius	Error flag	Control flag	$a_{desired}$
Column	13	14	15 - 16	17 - 19	20 - 22	23	24
Description	Mission duration	Constel number	Date created, date launched	$r_{x,y,z}$	$v_{x,y,z}$	Object class	ID

The parameters defined and tracked for each object throughout the simulation are defined in Table 1. The mean orbital elements are defined with semimajor-axis, eccentricity, inclination, RAAN, argument of perigee, and mean anomaly as: $[\bar{a}, \bar{e}, \bar{i}, \bar{\Omega}, \bar{\omega}, \bar{M}]$. B^* is an adjusted value of the ballistic coefficient of the satellite. The mass is denoted in kg, and radius is denoted in meters. The error flag is used for the internal propagation error state. The control flag denotes whether the object has control to stay at the desired semi-major axis $a_{desired}$ for the mission duration after launch. The constellation number denotes which constellation the object is part of, as defined in the constellation input file. The date created and the date launched are defined in modified Julian day (MJD). $r_{x,y,z}, v_{x,y,z}$ are cartesian states in inertial frame (ECI). The object class denotes the type of object, as described in Table 2. These definitions are consistent with those of the ESA MASTER database [50]. The satellite ID is defined for the purpose of tracking individual objects throughout the simulation.

Although all TLE objects are represented in the DISCOS database, some entries omit certain data. For MOCAT-MC, the DISCOS dataset is used for the physical parameters, launch date (or creation date for debris), and the type of object

*<https://www.space-track.org>

†<https://discosweb.esoc.esa.int>

‡<https://celestrak.org>

Table 2 Definition of object-class in MOCAT-MC

Class	1	2	3	4	5	6	7	8	9	10	11
Definition	PL	PL MRO	PL FD	PL D	RB	RB MRO	RB FD	RB D	D	Other D	Ukn

as one of the 11 categories defined by ESA. As the SatCat TLEs provide orbital parameters and type of object divided into Payload, Rocket Body, Debris, and Unknown, the objects with missing DISCOS data are sampled randomly from the PDF produced by the data from existing equivalent object type using a 2-D Gaussian fit. ESA’s DELTA model resamples the size and mass by assuming an aluminum sphere for the density to calculate the mass from the radius and vice versa, which often overestimates the density of fragmentation debris.

C. Launch Rate

The launch profile of new objects can be defined arbitrarily. Historical launch rates and object parameters can be used, such as the past n years of launches, where those objects are launched into the same orbits with the same object parameters, such as mass and shape. Some other studies have divided objects into constellation objects, which have a constant launch rate for replenishment level launches assuming some constant desired constellation size, while non-constellation objects would be launched at the historical rate over the n year period. Another method of launching would be completely arbitrary, where payloads with some lifetime are launched into the orbit of interest with randomized orbital parameters. Debris and rocket bodies can also be introduced per launch, as desired. For both of these scenarios, an assumed increase in launch rate per year can be specified, modeling some linear increase in launch activity with respect to time. The FCC and ITU filings for future megaconstellation have been compiled and are discussed in Sec. IV.D.

D. Atmospheric Density Modeling

LEO objects are strongly perturbed by the Earth’s upper atmosphere due to drag. Hence, accurate propagation of LEO objects requires an accurate estimate of the drag force caused by the Earth’s upper atmosphere. However, the ionosphere-thermosphere system is highly dynamic and is strongly influenced by solar and geomagnetic activities.

In lieu of a static exponential density model, in this work the Jacchia-Bowman 2008 (JB2008) density model is used [51]. The JB2008 density model is an empirical density model that is extrapolated based on past historical atmospheric density data to capture the statistically average behavior of the atmosphere under different solar and geomagnetic forcing. The main drivers for the JB2008 density model are a set of solar fluxes measured at different wavelengths and the temperature change due to the Disturbance Storm Time (DSTDTC) index. The set of solar fluxes captures the effects of solar activities; the DSTDTC index, on the other hand, captures the effect of geomagnetic activities on the thermospheric density field.

The difficulties in accurately predicting the long-term solar and geomagnetic indices are one of the main challenges with using the JB2008 density model for long-term prediction. The solar fluxes closely correlate to the solar cycle. A solar cycle lasts approximately 11 years and corresponds to the Sun's magnetic field cycle. Here, a moderately active solar cycle is assumed for all future solar cycles, using the observed solar indices for a moderately active solar cycle taken from [52]. At each propagation instance, the solar indices are sampled as independent Gaussian variables around the mean observed values, depending on the relative month in the solar cycle. On the other hand, a fixed DSTDTC value of 58k is used, which corresponds to the historical long-term mean DSTDTC value. However, note that the strength of the solar cycle tends to vary across different solar cycles and cycles over periods of high activities and low activities, and this is not reflected in our current assumption of consistently moderately active solar cycles.

Note that controlled payloads are propagated such that the semi-major axis will stay relatively constant. When a of such an object deviates by some defined amount from a_{desired} , a is simply updated to become a_{desired} to simulate station-keeping at the desired altitude.

The B^* value can be defined in several ways. When TLEs are supplied, the B^* value supplied from the catalog can be used. Note that the provided value may be negative and nonphysical, as this parameter is often a free parameter that is fitted to the sensor data to fit an orbit to create the TLEs. Figure 6 shows the distribution of some TLE sampling over a period of several days, showing the prevalence of negative B^* values and the magnitude with which the value varies from epoch to epoch. Horizontal lines denote the values of B^* that span more than the limits of the axis. This shows a wide range of the B^* values even for the same object within a week as reported by the TLE. For non-SGP4 propagators, B-star or AMR should be calculated separately. MOCAT-MC calculates the AMR from the physical properties of the objects, as noted in the ESA DISCOS database. A snapshot of the B^* values from TLEs from January 2023 is shown in Figure 31 in the appendix.

Alternatively, B^* can be recalculated from the physical characteristics of the satellite. This method will calculate the parameter as:

$$B^* = \frac{\pi r^2 \cdot C_D \cdot \rho_0}{2m} \quad (3)$$

where C_D is the ballistic coefficient and is simply defined as $C_D = 2.2$, r is the radius of the object, ρ_0 is the reference air density which is $0.15696615 \text{ kg}/(\text{m}^2 \cdot R_{\text{Earth}})$ [53], and the unit for B^* is R_E^{-1} .

To include the effects of space weather, in terms of solar and geomagnetic activities, on atmospheric density, the static exponential density model can be replaced by the static density model in [54]. Since the model mentioned above is valid within the range 150-1100 km, the reference altitude is assumed to be fixed at 150 km, for altitudes below 150 km, and at 1100 km, for altitudes above 1100 km. The comparison between these density models is seen in Fig. 7.

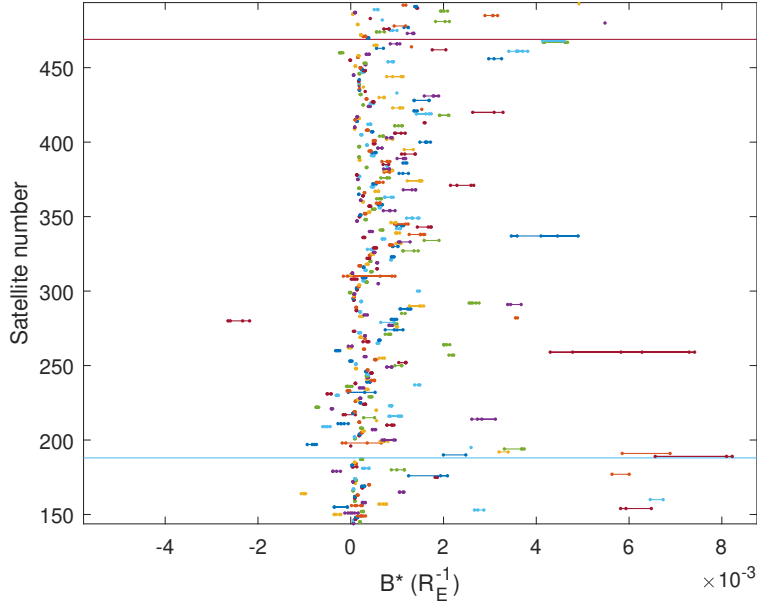


Fig. 6 Variability of B^* values from Space-track.org TLE's across a 5 day span

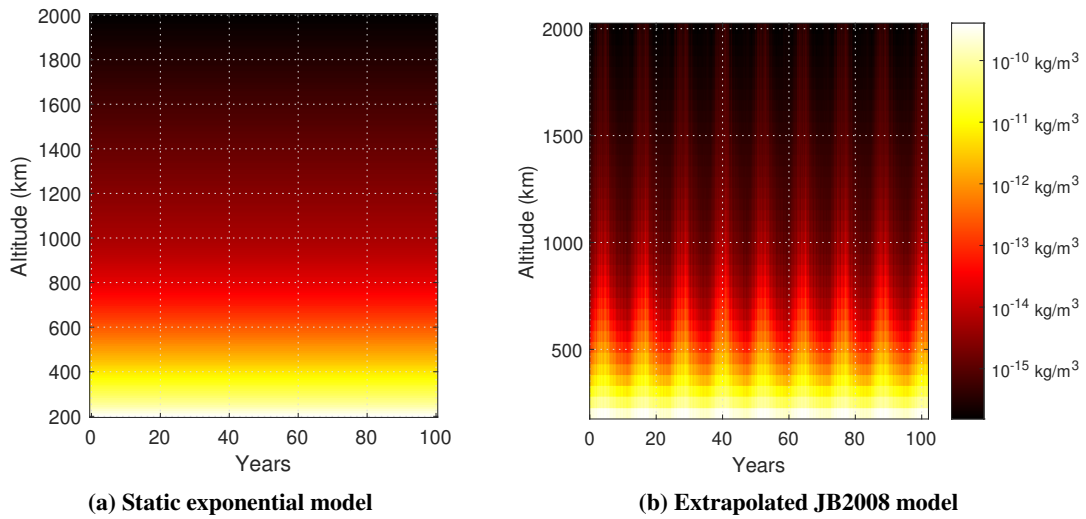


Fig. 7 Comparison between the two atmospheric models

E. Collision detection

There is a spectrum of methods to determine if a collision has occurred, ranging from deterministic methods to stochastic sampling-based methods. For the stochastic method, the Cube method has been used in numerous MC tools due to its scalability and simple implementation [31, 43], although some care is needed to adjust the algorithm parameters to allow realistic collision probability [55]. The computational scaling of Cube to n objects is $O(n)$.

Deterministic methods calculate the actual point of closest approach for each pair of satellites that are nearby. Adaptive propagation timesteps are needed to calculate the precise moment and distance between two objects, which imposes a significantly higher computational cost, and generally the computational scaling of these PCA methods to n

objects would be $O(n^2)$; however, methods that filter pairs of comparisons have been proposed in the literature that allow for complexity of $O(n^{1.5})$ [56–58]. A comparison between these methods is shown in the results section. Once a collision is detected, fragmentation dynamics using the NASA Standard Breakup Model (EVOLVE4) [42] is used as described in the next section.

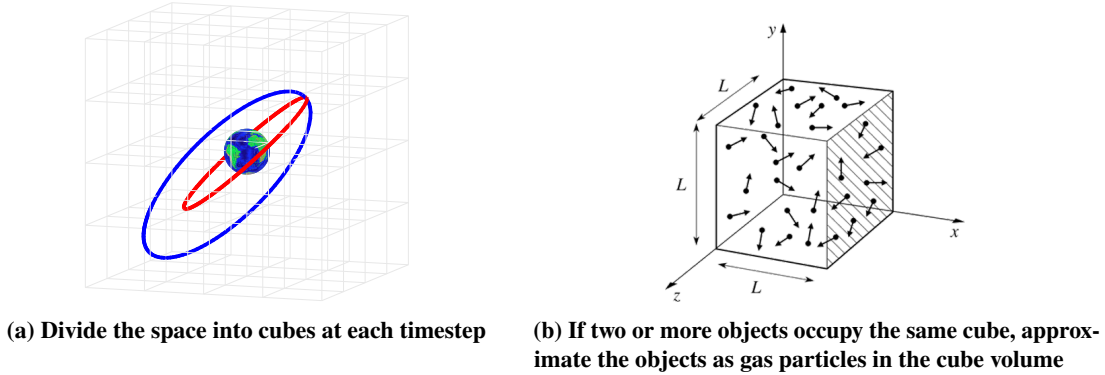


Fig. 8 The Cube collision detection scheme involves a two-step process: proximity filter prior to employing the gas particle collision model

The Cube method estimates the long-term collision probability by uniformly sampling the objects over time [43], which is explained here. The method treats any pair of objects to have a static probability of collision over a long period of time, and the collision probability is calculated for a particular moment in time when the objects are near each other. This is determined by discretizing the orbital space into cubes and flagging the two objects as close when they are in the same cube. At this point, the kinetic theory of gas is applied to determine the probability of collision. The probability of collision is calculated for any two objects that reside within a discretized cube concurrently, as

$$P_{i,j} = s_i s_j V \sigma dU \quad (4)$$

where s_i and s_j are the spatial densities of objects i and j in the cube, respectively, V is the relative velocity between the two objects, σ is the collision cross-sectional area, and dU is the volume of the cube. Note that this probability is the probability of collision per time, and the aggregate collision for the time step Δt is calculated at that time step as $P_{i,j} \Delta t$. The length of a cube for the proximity filter is often taken as 1% or less of the mean semi-major axis of objects, which is around 70 km for a population of LEO objects. The algorithm is described in detail in Fig. 8. The sensitivity and validity of using the Cube algorithm with various discretized time steps and cube size for collision detection modeling has previously been explored in the literature [55]. The relationship between cube resolution and the estimation of $P_{i,j}$ is explored later in the paper for the purpose of informing MOCAT-MC and its collision probability parameters. One benefit of the Cube approach is that the computational complexity is $O(n)$ as opposed to the exhaustive pairwise comparison that yields $O(n^2)$ for n objects.

F. Fragmentation Model

Fragmentation events in MOCAT-MC are simulated with the NASA SBM [42, 59]. The NASA SBM is a semi-empirical model based on evidence compiled from historical orbital data measured *in-situ* on-orbit as well as from terrestrial radar measurements and terrestrial hyper-velocity impact experiments. The model is deterministic and sample-based, and the samples are described by L_C the characteristic length, A/m the area-to-mass ratio, and Δv the ejection velocity in a random direction from the parent velocity.

The SBM specifies that the impact energy per target mass is

$$\tilde{E}_p = \frac{1}{2} \frac{m_c}{m_t} v_c^2, \quad (5)$$

where m_c is the mass of the chaser and m_t is the mass of the target, and impact velocity is v_c . The mass of the target is assumed to be greater than the mass of the chaser. In the SBM, a collision is considered *catastrophic* where the chaser and the target are completely fragmented when $\tilde{E}_p > 40$ J/g and *non-catastrophic* if not.

Ref. [60] reformulates the model into a PDF, where the number of objects produced with L that is greater than some lower bound L_0 is

$$N_L(L_0) = k L_0^{-\beta} \quad k, \beta > 0. \quad (6)$$

k and β are unitless parameters that depend on the type of fragmentation and the physical characteristics of the objects involved. Although the SBM does not inherently conserve physical quantities such as mass and kinetic energy [61], this formulation of the breakup model into a PDF allows for the conservation of mass and energy to be enforced.

The model takes as input the smallest characteristic length L_C for the generation of debris objects. The characteristic length is defined as the mean of the three maximum orthogonal projected dimensions of the object as $L_C = (L_x + L_y + L_z)/3$.

This is an input variable that can be adjusted; many simulations use the value 0.1 m as this is the commonly-used threshold for trackable objects in LEO. Note that L_C will be treated as an equivalent diameter d . Collisions between objects result in the generation of new objects within the simulation. The parameters of these new objects also follow the NASA SBM, as described in Eqs. 7 and 8. The number of fragments n_f of diameter $d > L_C$ can be computed as

$$n_f = \begin{cases} 6 c_s \hat{L}_C^{-1.6} & \text{for explosions} \\ 0.1 \hat{m}^{0.75} \hat{L}_C^{-1.71} & \text{for collisions} \end{cases} \quad (7)$$

where

$$\hat{m} = \begin{cases} \frac{m_t + m_p}{[\text{kg}]} & \text{for } \tilde{E}_p \geq \tilde{E}_p^* \\ \frac{m_p v_i^2}{1000[\text{kg} (\text{m/s})^2]} & \text{for } \tilde{E}_p < \tilde{E}_p^* \end{cases} \quad \text{with} \quad \tilde{E}_p = \frac{m_p v_i^2}{2 m_t} \quad (8)$$

Note that the symbol $\hat{\cdot}$ indicates normalized quantities, m_t and m_p are, respectively, the target (mostly derelicts or rocket bodies) and the projectile mass, v_i the relative velocity, \tilde{E}_p the specific energy of the projectile, and $\tilde{E}_p^* = 40$ [kJ/kg] the specific energy threshold for a catastrophic collision.

Particular attention should be paid to the scaling parameter c_s in Eq. 7. It is an event-specific calibration constant based on historic events, and an empirical correction for certain classes of fragmentation events, with $0.1 \leq c_s \leq 1.0$. For a mass between 600 kg and 1000 kg, the calibration factor is $c_s = 1.0$. However, past fragmentation events showed very different characteristics, thus the break-up models need to be calibrated. The implementation of the NASA SBM in MOCAT-MC is shown in the Appendix Fig. 30.

G. Area to Mass Ratio Calculation

According to the NASA SBM, the area-to-mass ratio A/m for new fragments is assigned according to a bimodal probability density function $p(\chi, \vartheta)$.

$$p(\chi, \vartheta) = \alpha(\vartheta) p_1(\chi) + (1 - \alpha(\vartheta)) p_2(\chi) \quad (9)$$

where $\chi = \log_{10}(\{A/m\}/[\text{m}^2/\text{kg}])$ is the area-to-mass parameter, $\vartheta = \log_{10}(d/[\text{m}])$, and $p_{1,2}$ indicates the normally distributed density functions. The parameter α , the means $\mu_{1,2}$, and the standard deviations $\sigma_{1,2}$ are calculated as stated in the NASA SBM. The effective cross-section A , function of the fragment diameter d is

$$A/[\text{m}^2] = \begin{cases} 0.540424(d/[\text{m}])^2 & \text{for } d < 1.67\text{mm} \\ 0.556945(d/[\text{m}])^{2.0047077} & \text{for } d \geq 1.67\text{mm} \end{cases} \quad (10)$$

The fragment mass is thus determined as

$$m = \frac{A}{A/m} \quad (11)$$

The model requires also to assign the imparted fragmentation velocities, which are sampled from a normal distribution characterised by the following mean value and standard deviation according to the SBM:

$$\begin{aligned}\mu_\nu &= 0.2\chi + 1.85 & \sigma_\nu &= 0.4 & \text{for explosions} \\ \mu_\nu &= 0.9\chi + 2.90 & \sigma_\nu &= 0.4 & \text{for collisions}\end{aligned}\tag{12}$$

where $\nu = \log_{10}(\Delta v/[m/s])$.

The propagation of debris clouds has also been an active area of research. Nominally, a covariance propagation model may be adapted, though the log-normal distribution of the number of objects and imparted ΔV in a collision is ill-suited to the multivariate Gaussian assumption for covariances. The evolution of debris clouds and their effect on key LEO orbits have been formulated and analyzed in [62–64]. Efficient cloud propagation has been explored through the DAMAGE model and other MC approaches [65–67]. The specific contribution of explosion and future collision fragments to the orbital debris environment showed the importance of mitigating fragmentation events [68, 69]. The probabilistic uncertainty of the lifetime of orbital debris was analyzed in [70–72]. The effect of thermospheric contraction on debris reentry has been modeled [33]. Empirical modeling of fragmentation events such as the Iridium-Cosmos collision and the 2013 ASAT test has validated some models [73–75].

The generation and propagation of the debris at various epochs using MOCAT-MC is shown in Fig. 9. The plot of the fragments shows 3 epochs: immediately after the collision, one revolution after, and two revolutions after the collision. Fragments are generated using the NASA Standard Breakup Model with $L_C = 10$ cm. The propagated locations of the original two objects are shown as red circles. As implemented in the NASA SBM, the magnitude of the ΔV imparted to each of the debris is stochastically assigned as a magnitude. For momentum conservation, it is assumed that the direction of the magnitude is uniformly distributed spherically, as is also implemented in the literature [60, 76, 77]. The result of the breakup model is also shown as a Gabbard plot in Fig. 10, with fragments divided into a range of sizes.

H. Active Payload Orbit Control

During propagation, each object is subjected to the effects of atmospheric drag, which causes the reduction of the semi-major axis a . On the one hand, this consequence is beneficial for LEO safety because it removes derelicts and debris, but on the other hand, it has to be counteracted by active satellites. Depending on the mission altitude and the solar activity level, perturbations, mostly drag effects, could require a satellite to perform station-keeping maneuvers even once per orbit. For current and future satellites, in particular those composing megaconstellations, electric propulsion seems to be the adopted hardware solution. This kind of propulsion system can provide a small level of thrust for a limited amount of time due to limitations in the available electric power. All of these factors, hardware solution, mission

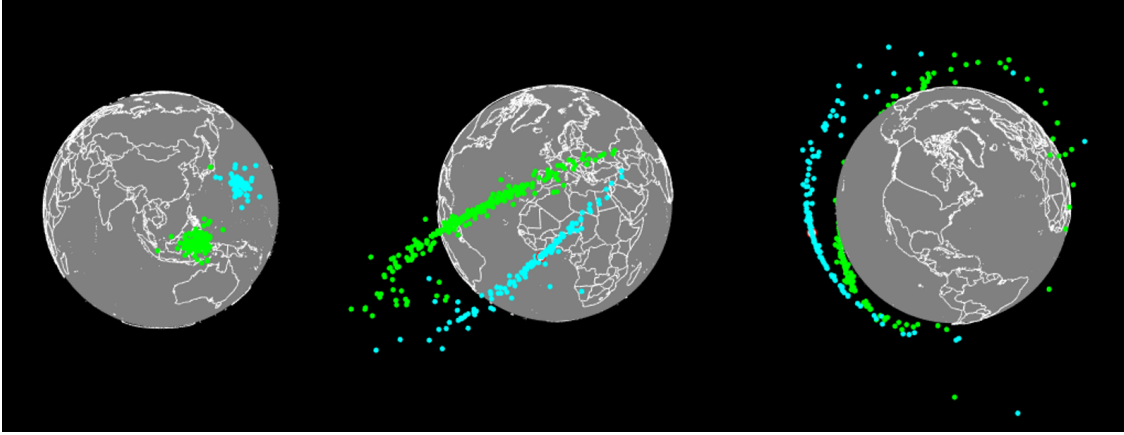


Fig. 9 Time-series graphical view of the debris generated from a collision between two payloads

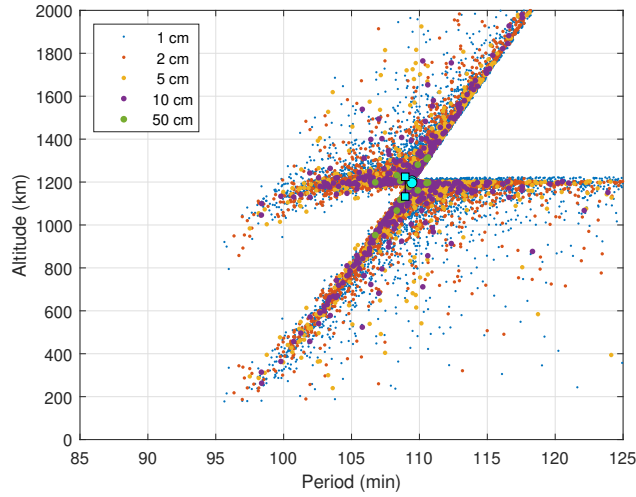


Fig. 10 Gabbard plot of debris 15 years after a collision

design, and mission constraints, could yield a satellite to split a maneuver into a small set of successive submaneuvers over each or a few orbits. Since orbit control modeling is not the main focus of the paper, the model considers the active satellite semi-major axis variation to be null. In fact, at each time step, all Keplerian orbital elements, except a , are propagated forward in time for active payloads. More accurate models are planned to be included in future works.

During propagation, each satellite is subjected to the effects of atmospheric drag. To model station-keeping maneuvers for active satellites, a threshold on the semi-major axis variation Δa_{thr} has been set. The simplified maneuver consists of adjusting the current semi-major axis $a_{\text{current}}(t)$ (time dependent) to the initial and desired value a_{desired} whenever, during propagation, the following condition is verified.

$$a_{\text{desired}} - a_{\text{current}}(t) > \Delta a_{\text{thr}} \quad (13)$$

Moreover, active satellites are supposed to perform collision avoidance maneuvers with a certain probability of

failure, indicated by α in case the satellite encounters a noncooperative species (rocket bodies, derelict or debris), while with α_a if the encounter is between two active satellites. The resulting probability of collision, computed with Eq. 4 is therefore pre-multiplied by one of these two factors as:

$$P_{i,j} = \begin{cases} \alpha_a P_{i,j} & \text{active-active encounter} \\ \alpha P_{i,j} & \text{otherwise} \end{cases} \quad (14)$$

Although these terms are defined by the user, realistically $\alpha_a < \alpha$, as a pair of satellites is assumed to have a greater chance of successfully performing a collision avoidance maneuver through coordination compared to an active satellite against debris.

Despite the large number of potential conjunction events, there has never been an active-on-active collision, leading to a historical trend of $\alpha_a = 0$. Even an active-on-derelict conjunction is quite rare with such safeguards and warnings in place. The first collision between satellites was the Iridium-Cosmos collision in 2009, although the policy of issuing CDMs using high-quality data had not been implemented then [78].

Although there has been a rapid growth in controlled payloads launched into LEO, collisions between an active satellite have not happened yet. However, near-conjunctions for active satellites are a daily occurrence. Since the first Starlink satellites were launched in 2019, they have had to perform 50,000 collision avoidance maneuvers by 2023, and at the current rate, the Starlink satellites will have to maneuver more than a million times in a half-year span by 2028 [79]. The 18th and 19th Space Defense Squadrons have issued more than 170 million conjunction data messages (CDM) for more than 3 million conjunction events between January 2016 and December 2021 [80]. With an increase in the number of constellation operators, so does the need for proper coordination between the operators. The increased complexity may result in the first ever collision between two active payloads.

I. Future Constellation Traffic

Future constellation traffic is described by specifying a few parameters per constellation in an external file that is ingested by the simulation during the setup phase. Several parameters must be entered for each constellation. The altitude and inclination are given for each shell or generation of the constellation and the number of satellites already in orbit at the start of the epoch. Satellite parameters such as mass, radius, and mission life are also required, although missing information will default to using Starlink Gen 1 specifications. The date of start and end of the build-up phase must be supplied to calculate the launch rate during the build-up phase, where a linear build-up phase is assumed. Throughout the operational phase of the constellation, the appropriate replenishment satellites are launched for the satellite that has reached the end of life. The end of operation date can be supplied to the constellation, after which no more replenishment satellites are launched. The constellation company index can be supplied to group the separate

shells and phases into the same constellation. Intra-constellation collision avoidance efficacy, for example, can be specified such that the collision within a company's constellation is different (usually assumed to be lower) than that of inter-constellation collision avoidance efficacy due to better coordination within an organization.

III. Validation

A. Validation against the IADC study

The Inter-Agency Space Debris Coordination Committee (IADC) in 2009 had several space agencies use their MC tools to compare the performance for a strict future scenario [81]. Several models contributed and were compared with each other: ASI: Space Debris Mitigation long-term analysis program (SDM), ESA: Debris Environment Long-Term Analysis Model (DELTA), ISRO: KS Canonical Propagation Model (KSCPROP), JAXA: LEO Debris Evolutionary Model (LEODEEM), NASA: LEO-to-GEO Environment Debris Model (LEGEND), UKSA: Debris Analysis and Monitoring Architecture for the Geosynchronous Environment (DAMAGE).

A 2009 baseline environment for debris 10 cm and larger was provided by ESA. The future space traffic model was based on a repetition of the historic 2001-2009 space traffic. Each participating member used its own solar flux projection model. A catastrophic collision was defined as one characterized by an impactor's kinetic energy to the target mass ratio of 40 J/g or greater. A future post-mission disposal (PMD) compliance level of 90% was assumed for both the spacecraft and launch vehicle stages. The initial simulation epoch was 2009 and was simulated for 200 years. The initial object count was 17,070 based on the MASTER database, which included payloads, derelict objects, rocket bodies, and debris. Launches were repeated for launches between the years 2002 and 2008. The payload lifetime was assumed to be 8 years and no collision maneuvers were assumed for any objects. No explosions were assumed either.

The six models yielded similar qualitative results and confirmed the instability of the current LEO object population. The six member models revealed a steady increase in the > 10 cm population, despite an assumed global PMD level of 90%, with a rate of catastrophic collisions varying from once every 5 to 10 years. The majority of catastrophic collisions occurred near the 800 km and 1000 km altitudes due to high concentrations of space objects there. The study concludes by noting that compliance with existing national and international space debris mitigation measures will not be sufficient to constrain the future population of LEO objects. To stabilize the LEO environment, more aggressive measures, especially the removal of the more massive nonfunctional spacecraft and launch vehicle stages, should be considered and implemented in a cost-effective manner.

MOCAT-MC was used to run the same scenario to validate its results against the six models used in the IADC study. Although the specifics of the simulation data were not available, the best estimates were used to emulate the same scenario. For example, the initial population of the IADC study starts with 17,074 objects in LEO, though the TLEs available for the same epoch yielded around 9,874 objects. To start with the same number of objects with similar

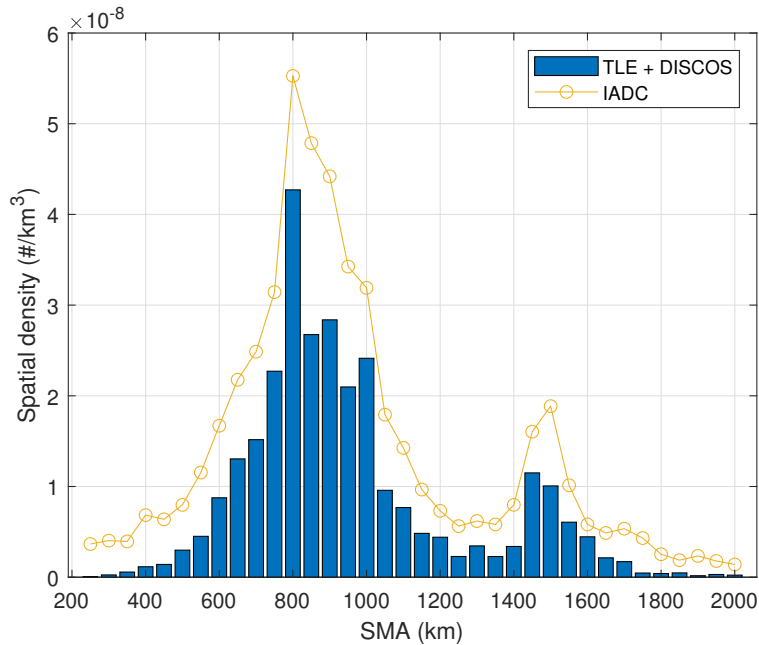


Fig. 11 Initial population spatial density for IADC study vs TLE for scenario epoch May 2009

altitude density profile, a total of 7,200 debris were added with the orbital and physical properties randomly selected from existing debris. The altitude of the additional debris was selected to match the initial spatial density of the initial population provided in the study as seen in Fig. 11. Although the study was limited to trackable objects, the additional population was likely in the smaller objects compared to the tracked objects with orbits in the TLE catalog. To account for this size discrepancy in debris sampling, the characteristic length of the expanded initial population of TLE/DISCOS was reduced by a factor of 1.5. In addition, the PMD scheme assumed within MOCAT removes the object from the simulation when PMD is successful.

The summary of the MOCAT-MC validation exercise using the IADC study scenario is shown in Table 3. The comparison of the total population between MOCAT-MC and the models used in the IADC study is shown in Fig. 12, and the cumulative catastrophic collisions and the altitude of catastrophic collisions are shown in Figs. 13 and 14, respectively. MOCAT-MC performed similarly to those of the IADC study for these key metrics.

The details of this MOCAT-MC validation scenario are shown in Fig. 15. The population per object class shows that the number of debris dominates the > 10 cm population and contributes as the main source for the increase in the total object count. The total population for some individual simulation is shown in gray for the population. The intact objects (payload and rocket body) are relatively stable. The collision number shows the relative occurrence between catastrophic collisions and all collisions.

The bottom portion shows the cumulative number of collisions, with the solid line denoting any collisions, whereas the dotted line shows only the catastrophic collisions. In this scenario, most collisions are deemed catastrophic.

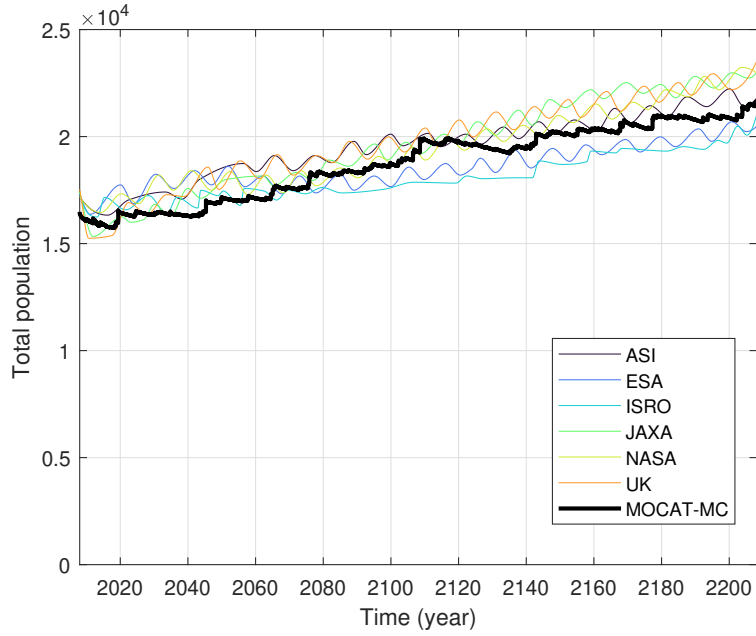


Fig. 12 Comparison of total population between MOCAT-MC and IADC models [81]

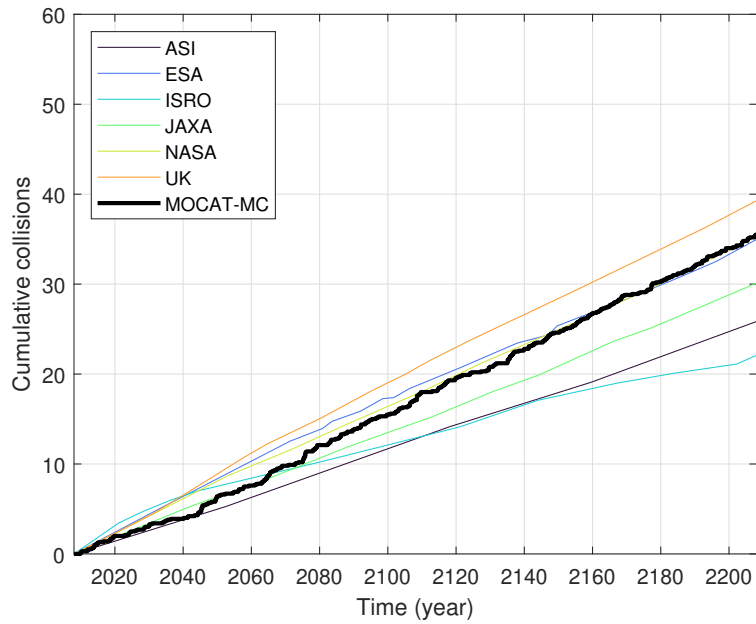


Fig. 13 Comparison of cumulative catastrophic collisions between MOCAT-MC and IADC models

IV. Results and Discussion

Many of the sub-functions were varied to understand the sensitivity of the simulation results on the various input parameters to the model.

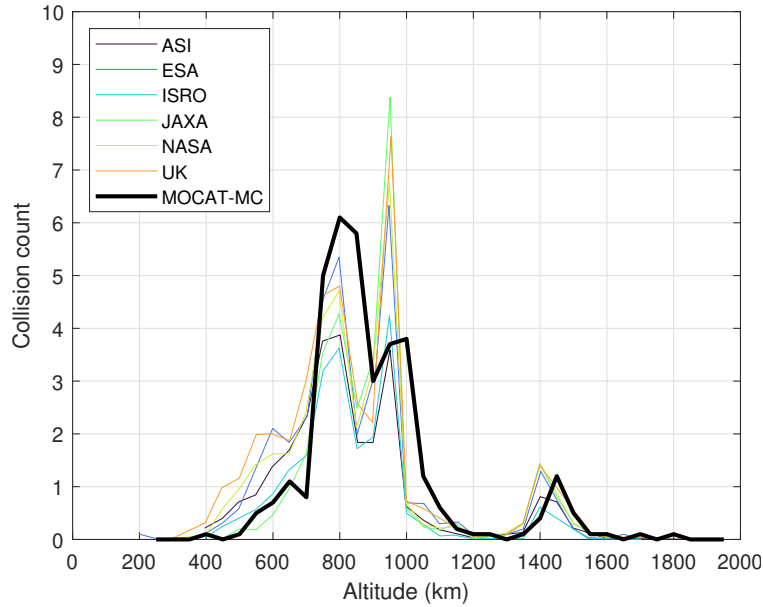


Fig. 14 Comparison of altitude of catastrophic collisions between MOCAT-MC and IADC models

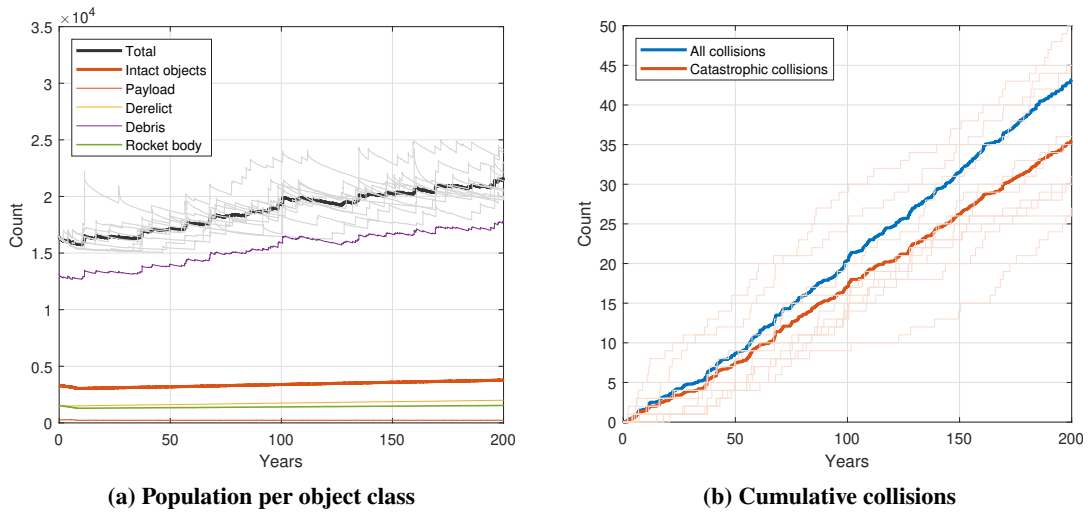


Fig. 15 Details of the MOCAT-MC results for the IADC scenario

A. Benchmarking

The computational resources required to run MOCAT-MC are shown in Fig. 16 for a range of 100-year simulations on the SuperCloud system [82], with Intel Xeon Platinum 8260 processors. Within MOCAT-MC, both the collision detection algorithm through Cube and the propagator scale as $O(n)$, which is shown in the computational duration. Populations of 17,000 to 10^7 were run. MOCAT-MC is a single-threaded simulator – multiple threads and cores would allow for simultaneous runs of different MC simulations, but it will not inherently improve the run time for a particular MC simulation.

Table 3 Comparison between IADC study results and MOCAT-MC runs of the same NFL scenario

Agency Model	ASI SDM	ESA DELTA	ISRO KSCPROP	JAXA LEODEEM	NASA LEGEND	UKSA DAMAGE	All IADC -	MIT MOCAT-MC
Runs with $N_{2209} > N_{2009}$	88%	75%	90%	88%	89%	94%	87%	92%
Change in Population	+29%	+22%	+19%	+36%	+33%	+33%	+30%	+35%

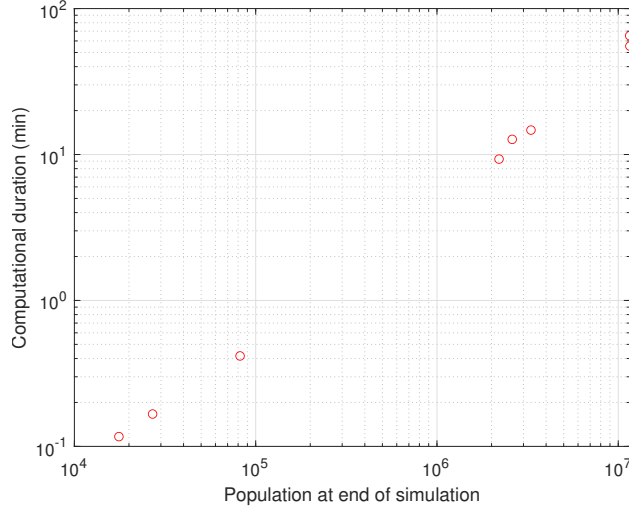


Fig. 16 Simulation duration for MOCAT-MC

B. Extrapolated and No Future Launch cases with 2023 epoch

Two scenarios are run with MOCAT-MC to compare the effect of future launches on the trackable orbital population in LEO with scenario epoch at Jan 1 2023:

- Extrapolation of the recent launch traffic, explosion rates, and post-mission disposal rates
- No future launches scenario where no launches take place after 2022.

The SatCat TLEs were used for the orbital parameters of the trackable debris population with reference epoch Aug 1 2022, while the ESA DISCOS database was used for parameters such as the objects’ size, mass, object type and launch date. Only objects with perigee between 200 km and 2000 km were considered. This initial population profile is shown in the Appendix Table 5.

Table 4 Scenario parameters

Scenario	$T_{scenario}$	Δt	a_p limit	Launch profile	$\mathbb{E}[P_{explosion}]$	P_{PMD}	PL lifetime
NFL	100 years	5 days	$200 < a_p < 2000$	n/a	n/a	n/a	n/a
Extrapolated	100 years	5 days	$200 < a_p < 2000$	repeat 2017-2011	RB: 2.3 / yr	0.4	8 years

All simulations were run for 100 years, and 100 Monte Carlo simulations were run on the MIT SuperCloud High

Performance Computing cluster [82]. The explosion rate for rocket bodies and payload lifetimes is taken from the ESA Annual Report [14]. There are 1594 objects from the TLE catalog that are not depicted in this initial population, as they have an SMA greater than 2000 km, whose perigee is within the altitude limit. Figure 17 shows the evolution of the total population of the simulation, as well as the cumulative collisions over the 100-year simulations. The dotted lines above and below denote the 3σ boundaries. The growth of objects can be seen even for the NFL case.

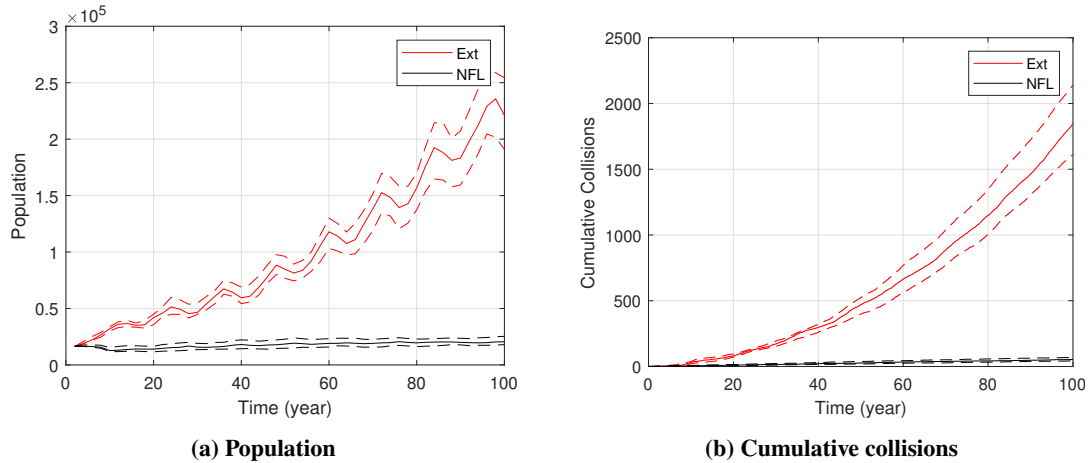


Fig. 17 Extrapolated and No Future Launch Scenarios for Epoch 2023

It is difficult to compare the computational duration required by MC models, as they are not typically disclosed in the literature. Discussions with authors and researchers using these models reveal that MC simulations can take days to weeks [83]. However, a comparison of the maximum population modeled is disclosed in the published literature. Although not all published work aims to maximize the number of objects to model, some comparison and references are shown in Fig. 18, which demonstrates the computational efficiency of MOCAT-MC. As shown in the earlier sections, simulations of more than millions of objects will be necessary to model the full proposed future megaconstellations. Measuring the effect of lethal non-trackable objects will also require high population simulations.

C. No Future Launch Cases from the Past

The No Future Launch case shown in the Validation section shows growth in the number of objects and in the number of collisions despite no new launches occurring. The literature has shown that MC methods point to the fact that the LEO environment was in an era of unabated growth for decades prior [14, 31, 35]. Using the same methodology as in the previous section with the combined dataset between the TLE catalog and the DISCOS database, the future LEO environment is simulated at different epochs in the past. The NFL case is run for every year starting in the year 2000 with the cataloged objects at those epochs and removing all future launches to see the growth or decay in the number of objects.

January 1 of each scenario epoch year is used for the initial population of objects for the LEO objects, which

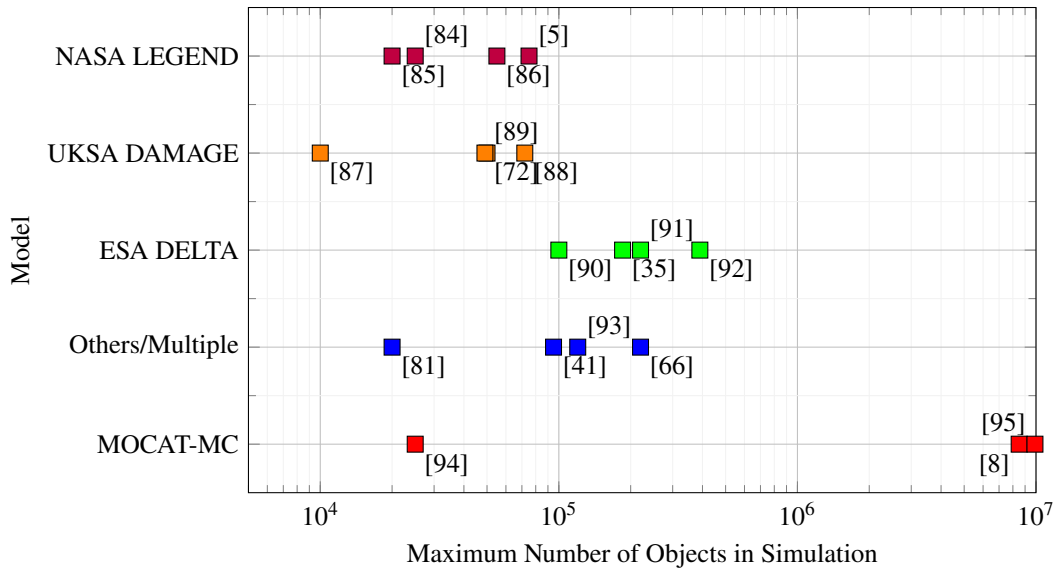


Fig. 18 Comparison of population modeled in MC simulation tools

inherently limited the initial population to the tracked objects. All payloads were assumed to have a mission lifetime of 8 years, after which they undergo PMD with 90% success rate. Collision avoidance failure rate of $\alpha = 0.01$ and cube resolution of 10 km. No new objects were introduced into the environment other than through collision dynamics.

The results are summarized in Figs. 19 and 20. All of the simulations show a substantial growth from the initial population, which indicates that even without future launches, the unabated growth of objects is seen at least as far back as the year 2000 when there were 5000 tracked objects in orbit.

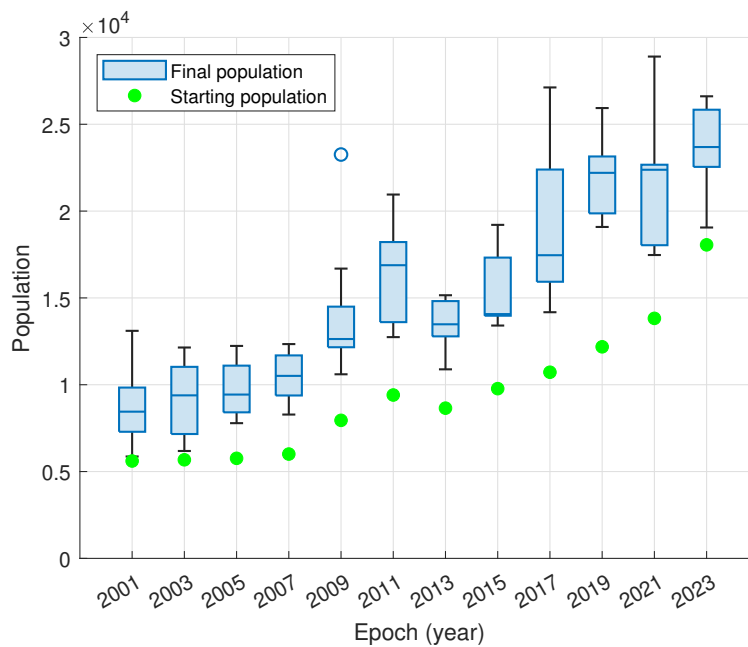


Fig. 19 Object count for NFL cases starting at different epochs simulated for 100 years

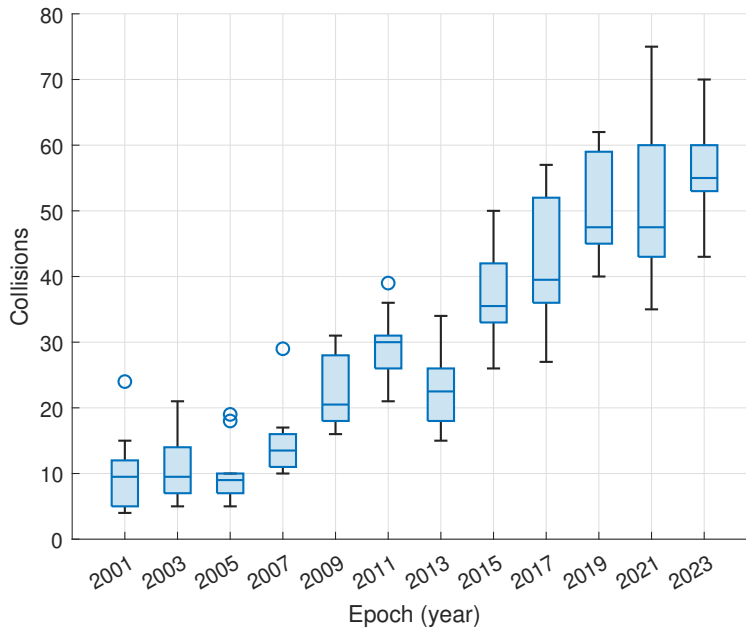


Fig. 20 Cumulative collisions over 200 years at various epoch for the NFL cases

The results show that the growth in the number of objects is consistently present even with epoch in the year 2000, showing the importance of debris mitigation with any population. Of note are the more recent years, where the total count of trackable objects remain roughly steady compared to previous years despite the higher initial population count; in these scenarios, the Starlink satellites have begun to populate, taking up a significant portion of the initial population for those epochs. These active satellites will have been removed entirely from the environment within 8 years of the epoch, other than the few that remain as derelict satellites after failed PMDs. Compared to other satellites, the average lifetime for these active payloads at the simulation epoch are much shorter; therefore, the effect on the space environment is much less. For two scenarios with the same number of population, the one with a greater proportion of active satellites that can CAM and PMD will yield a safer and sustainable long-term LEO environment.

The population divided into altitude is shown for the 2023 NFL case in Fig. 21. The dense region in the first few years around 550 km denotes the numerous Starlink satellites which mostly PMD after its mission lifetime, which is also seen in the payload population in the Appendix. The number of objects above the 700 km range continues to grow, though most objects below deorbit relatively quickly. The growth in the 1000 km and 1400 km altitude region is seen, where many derelicts and debris exist and are relatively unaffected by atmospheric drag. The altitude regions with higher density start to merge as collisions increase the number of objects and add objects to a range of altitudes around the collision. The difference between the initial and final population is more pronounced in the comparison shown in Fig. 22, where the cumulative collision occurrence is also shown.

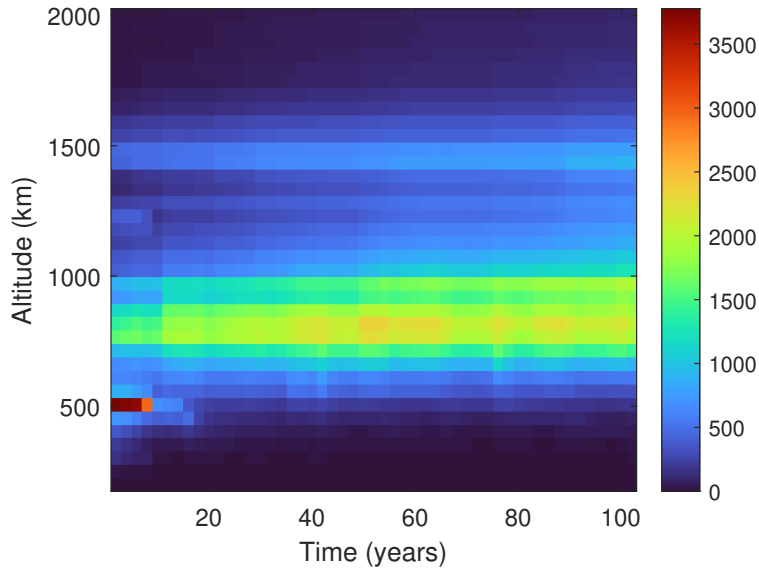


Fig. 21 Total population per altitude for the NFL case with epoch at 2023. Altitude is binned at 50 km, and time is binned yearly.

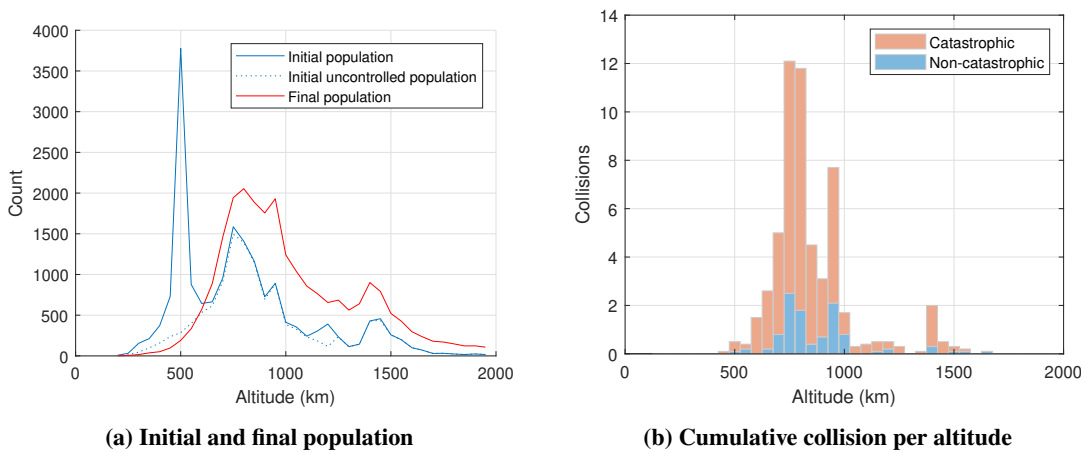


Fig. 22 NFL case with epoch at 2023. Altitude is binned at 50 km.

D. Future Traffic with Megaconstellations

Megaconstellations are large networks of interconnected satellites that are designed to provide various services, including global broadband internet coverage, Earth observation, and communication capabilities. Two prominent examples of proposed megaconstellations are SpaceX’s Starlink and OneWeb. The race to deploy megaconstellations is driven by the potential benefits of widespread internet access, improved communication infrastructure, and enhanced Earth observation capabilities.

It is impossible to forecast the exact state of LEO traffic and launches in the upcoming decades. The best estimate of megaconstellation data can be compiled from various sources, particularly governmental and regulatory bodies such as the FCC and ITU as well as press releases. As of writing, there are more than 50 megaconstellations – defined

as constellations comprising more than 1000 satellites – that have been credibly proposed [96–98]. Of these, only a few have operational satellites at the time of writing. As these are all commercial ventures, the technology roadmap, market conditions, and consumer demand make the forecasting of successful launch and operation of megaconstellations difficult.

A few examples of megaconstellations are described below. These examples highlight the growing interest in megaconstellation projects across various countries and industries, notably in the internet connectivity and remote sensing applications. Even in the past few years, many prominent megaconstellation projects that have filed with the ITU and/or FCC have been canceled or merged with other efforts. Future launches and traffic due to megaconstellation should be taken as estimates at best; however, this list gives a general overview of launches to expect.

SpaceX Starlink * SpaceX initiated the Starlink project in 2015 with the goal of creating a satellite network capable of delivering high-speed, low-latency internet access worldwide. The primary motivation behind Starlink was to bridge the digital divide and provide reliable internet connectivity to underserved regions. The constellation would consist of thousands of small, low-Earth orbit (LEO) satellites that create a mesh network. SpaceX began launching Starlink satellites in batches starting in May 2019. As of September 2021, SpaceX had already deployed thousands of satellites, and beta testing of the Starlink service had begun in select regions.

Eutelsat OneWeb † OneWeb is another megaconstellation project that aims to provide global broadband internet coverage. Founded in 2012, OneWeb intended to build a network of LEO satellites that could deliver internet services to remote and underserved areas. The project was supported by several notable investors, including SoftBank, Qualcomm, and the Government of the United Kingdom. OneWeb faced financial challenges and had to file for bankruptcy in March 2020. However, the company was subsequently acquired by a consortium consisting of the British government and the Indian company Bharti Global. This acquisition provided the necessary funding to continue the project. OneWeb resumed satellite launches in December 2020 and has since progressed with its deployment plans.

Amazon Project Kuiper ‡ Project Kuiper is Amazon’s venture to create a megaconstellation of satellites to provide global broadband internet coverage. Announced in 2019, the project aims to deploy a network of more than 3,200 LEO satellites. Like other megaconstellations, Project Kuiper’s objective is to deliver affordable, low-latency internet services.

Telesat Lightspeed § Telesat, a Canadian satellite operator, is working on its own megaconstellation known as Telesat Lightspeed. The project aims to provide broadband connectivity worldwide using a network of approximately 300 LEO satellites. Telesat’s focus is on serving both residential and commercial markets, offering high-speed internet access, enterprise connectivity, and government services.

*<https://www.starlink.com/>

†<http://oneweb.net/>

‡<https://www.aboutamazon.com/projectkuiper>

§<https://www.telesat.com/leo-satellites/>

E-space Semaphore-C * Greg Wyler's company E-space made headlines when it registered 327,000 satellites using Rwanda as the registration authority through the ITU in 2021. In June 2023, the company filed another constellation *Semaphore-C*, which is a constellation of 116,540 satellites orbiting between 414 and 600 km altitude, registered in France. Due to the recency of this addition, E-Space's constellation will not be part of this analysis. Note that numerous other studies and literature have ignored this constellation due to the perceived lack of credibility that the constellation will launch in its entirety. The proposed constellation of more than 400,000 satellites would dwarf the total number of other proposed megaconstellations. This highlights the academic and industry sentiment that regulatory filings are necessary but not sufficient to be used as credible sources for future LEO traffic.

The future launch model used in this scenario is listed in Table 6, and totals more than 82,000 satellites in operation just from the megaconstellations alone. The missing mass and radius represented with a '-' used the Starlink satellite as the surrogate (260 kg and 2 m radius), while the start and finish years were set to be the latest dates for the other constellations with some data (2035 to 2055 for Guanwang). Figure 23 visualizes the launches. Note that the replenishment launches are not shown in this figure. An average of $n/yr_{\text{missionlife}}$ satellites per year will be required to launch in order to maintain the current number of satellites n .

Three subsets of these megaconstellation launch scenarios are also chosen to be simulated. *Case 1*: all of the filed megaconstellations as shown in Fig. 23, which totals 84139 operational megaconstellation satellites. *Case 2*: just the constellations filed by Starlink, Kuiper and OneWeb, all of which have some constellation presence as of Jan 2024. This totals 44716 operational megaconstellation satellites. *Case 3*: which comprises of just Starlink v1, v1.5, Kuiper and OneWeb. Compared to Case 2, this case removes the largest megaconstellation proposed considered, which is Starlink v2. This totals 22228 megaconstellation satellites.

The simulation results for the three cases along with the case of no future launches are shown in Fig. 24. The growth in the number of objects is clearly seen in all cases. Notable are the S (payload) and D (derelict) plots in Fig. 25 – the number of objects increases with increasing launch scenarios, but at the highest number of launches, the number of payloads starts to decrease, despite the 1% probability of failure to avoid a collision. That effect is more pronounced in the derelict class, where such avoidance is not possible, and the number of derelict objects starts to dwindle after 100 years. In these charts, it is also seen that the number of objects is likely to grow even without new launches. This is in line with the findings from the literature and highlights the urgent need to limit the creation of derelict objects through higher PMD rates and effective collision avoidance maneuvers to limit fragmentation events. The temporal evolution of the population per altitude is shown in Fig. 26. This clearly shows the large amount of accumulation above 1000 km region.

The population difference between objects above and below 700 km shows the accumulation rate between the higher and lower altitudes. Figure 27 shows the comparison for each of the four cases, with the dashed line denoting the

*<https://www.e-space.com/>

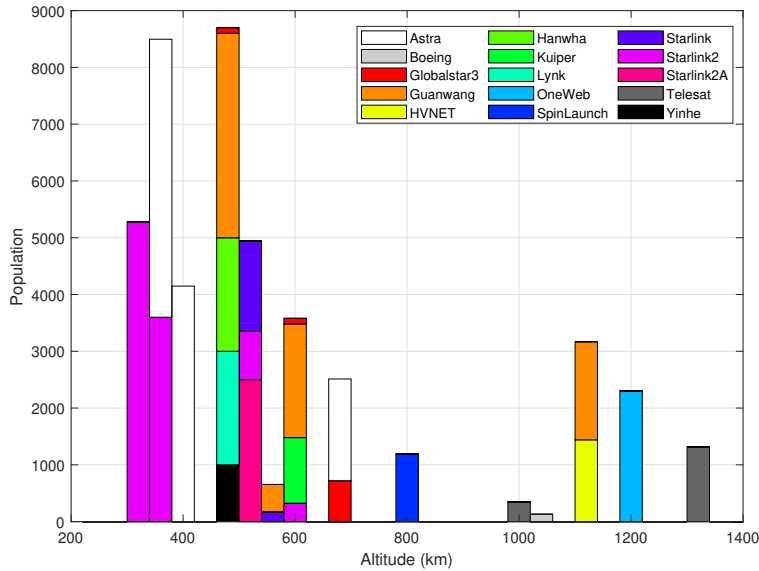


Fig. 23 Modeled total operational population per megaconstellation

population below 700 km and the solid lines denoting the population above 700 km. Despite much higher launches occurring below 700 km, the population below 700 km remains largely steady and low, whereas the higher altitudes grow continuously. This is pronounced even for the *No Future Launch* case. The lower altitude also exhibits undulation of the population as a result of the thermospheric expansion and contraction that follow the solar cycle. The comparison of launching into only lower-altitude shells is explored in the next section.

E. Megaconstellation launches with limited altitudes

To see the effect of megaconstellation launches at higher altitudes, a subset of the total megaconstellation case was launched and analyzed. The altitude limits of < 600 km (total 59336 operational), < 700 km (65408), < 900 km (66598) were chosen. The launch altitudes of the megaconstellations can be found in Fig. 23. The same parameters as in the previous section were used, except for the launched subset.

The collision and population statistics from the < 700 km constellation case is shown in Fig. 28, while the other cases are shown in the Appendix. The comparison between these altitude-limited constellations is shown in Fig. 36. It is clearly seen that the growth of the debris population and the collision rates are dominated by higher orbits. Despite the much fewer objects launched > 700 km, the total collision number across the 200-year simulation is more than halved. Note that for this analysis, the same PMD efficacy rate is used for all constellations. That is, the frequency of successful removal from the environment after the mission life of the active payload is the same for all payloads of the same type regardless of the altitude of the constellation. The more numerous population for the > 700 km launch scenario is due to the derelict satellites in higher orbits that remain in the environment for much longer due to lower atmospheric drag.

For comparison, Fig. 29 shows the population when the > 700 km constellations are launched. Although the

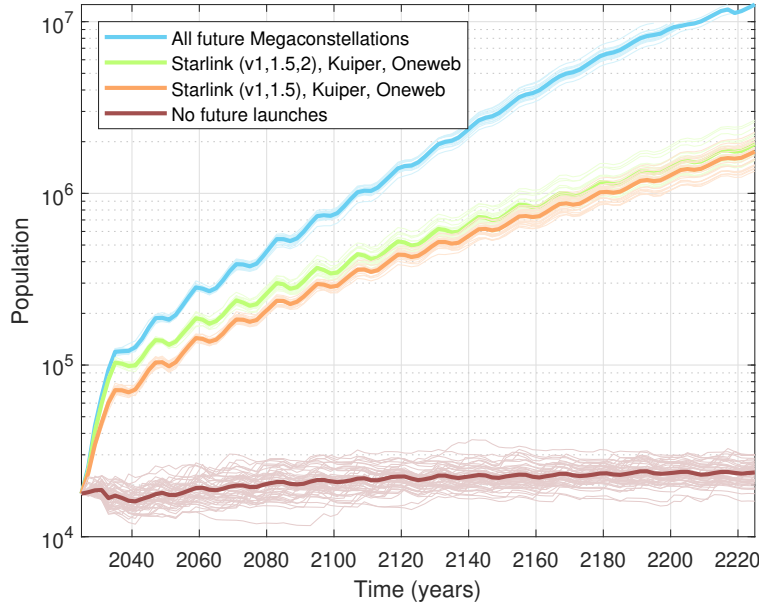


Fig. 24 Total population in LEO with future megaconstellation launches

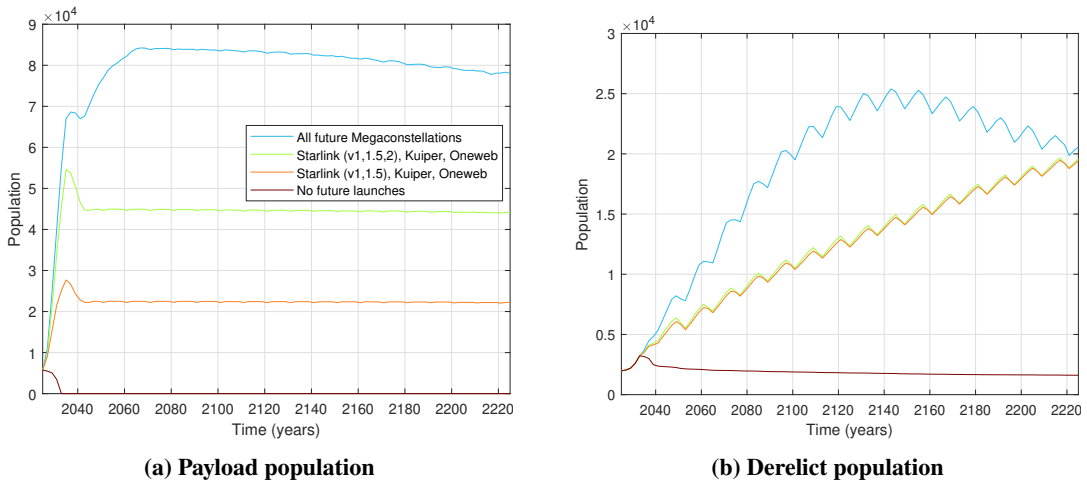


Fig. 25 Payload and derelict population with various future megaconstellation launch models

operational satellites for the > 700 km megaconstellations are about 1/4 of the < 700 km case, the population growth is much more pronounced. The reduced drag effect is clearly seen, with the debris population from the 800 km region persisting throughout the simulation duration. In Fig. 29(b), the dotted lines denote the uncontrolled objects, including derelict and debris objects. The solid line is the total number of objects. The difference between the solid and the dotted line is the controlled payload population, where Starlink’s contribution to the current population (Initial population) is clear around 500 km. This comparison shows the relative difference between the debris population and the payload population. The low-altitude constellations are able to have a much higher payload-to-debris ratio, enjoying a lower debris environment due to the atmosphere while also lowering the collision avoidance operational burden. Higher orbits,

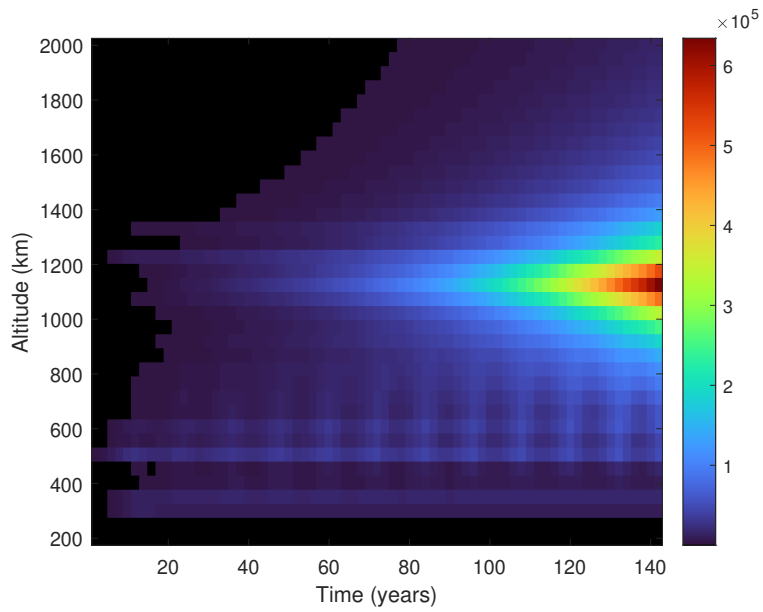


Fig. 26 Total population per altitude for the all future megaconstellations case. Altitude is binned at 50 km and time is binned yearly.

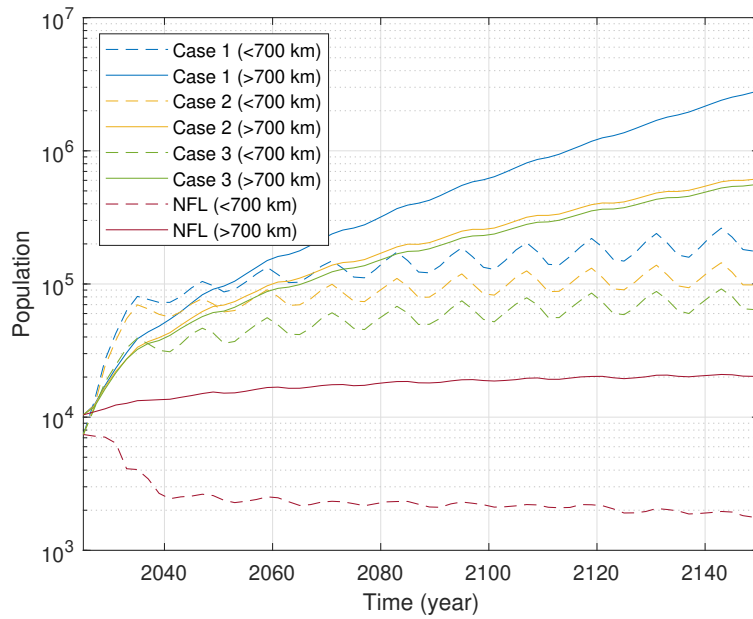


Fig. 27 Total population below and above 700 km altitude for the four future launch cases

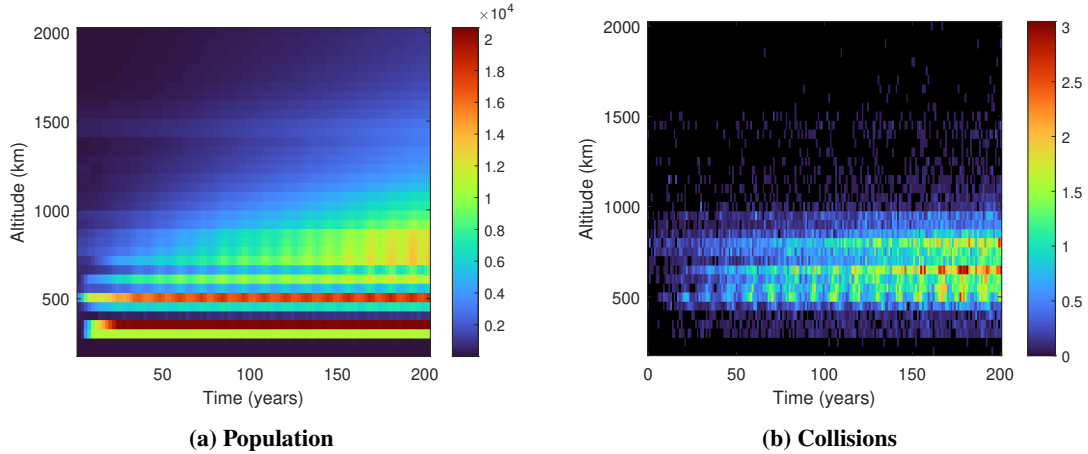


Fig. 28 Megaconstellation launches limited to < 700 km

despite having the same PMD and α collision avoidance efficacy, exist with a much higher debris-to-payload ratio as the debris accumulates. This shows that debris mitigation efforts through higher PMD and effective collision avoidance will be crucial to maintaining a viable orbit regime for higher altitudes.

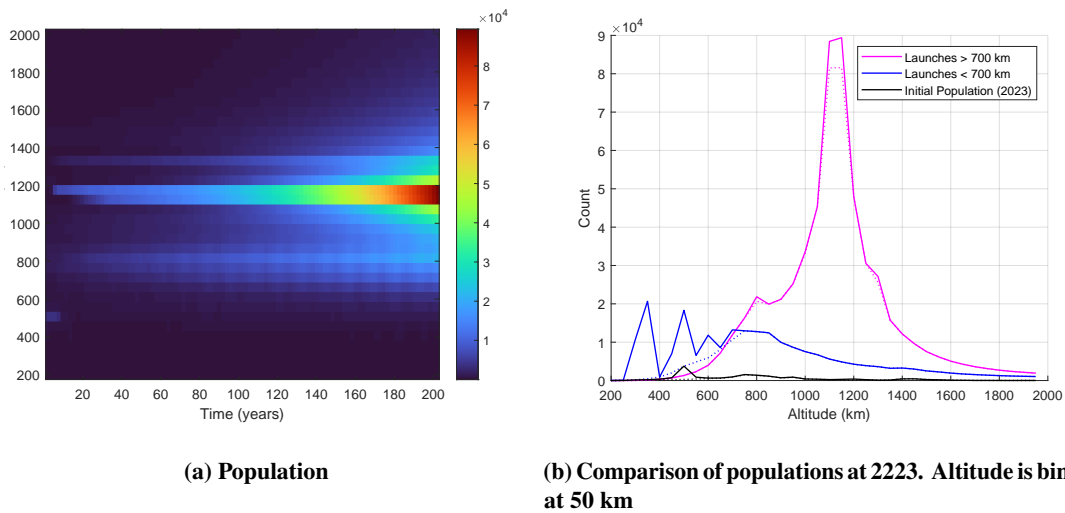


Fig. 29 Megaconstellation launches limited to > 700 km

V. Conclusions

As access to space is becoming easier and with the accelerated pace of launches into LEO, it is imperative to be able to model the future space environment and understand the various inputs that can shape the future. This paper describes a novel open-source Monte Carlo-based method to simulate the evolution of the LEO population called MOCAT-MC. The tool efficiently models the evolution of the orbital population characterized by dynamics such as launches, collisions, explosions, deorbit methods, and more. This Monte Carlo tool is flexible in its modeling fidelity with several options for

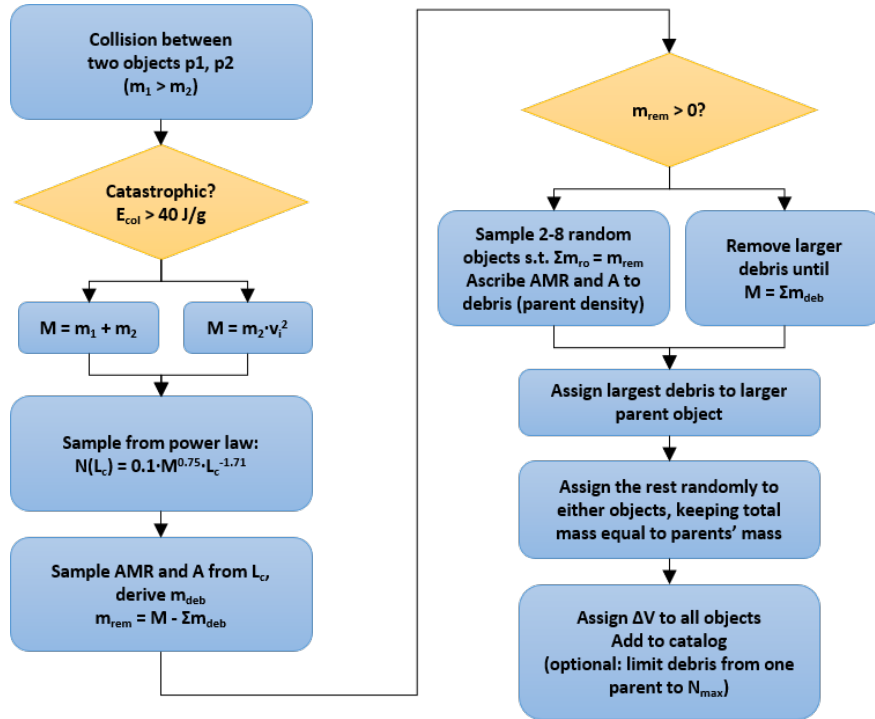


Fig. 30 NASA Standard Breakup Model as implemented in MOCAT-MC

the propagator, initial simulation population, and launch profiles. A sampling-based collision model is used and its sensitivity to input parameters is explored. Statistical convergence is tested, and the output result has been validated against six other models in the literature with which MOCAT-MC shows good agreement. Additionally, MOCAT-MC is able to simulate up to 20 million objects over a period of 200 years, improving on the previous state-of-the-art, which was 400K objects over the same period. Historical look at the no-future launch cases shows that the LEO population without any new launches since 2000 may have continued to grow and has only accelerated with the increased population since then. A future launch case involving all megaconstellations filed with the ITU and FCC is explored, where the number of objects > 10 cm grows to tens of millions of objects. These results underscore the importance of a multitude of debris mitigation strategies that include international policies and technological solutions. The simulation results show some important conclusions: the higher-altitude accumulation of orbital debris is much faster than that of the lower altitudes and warrants careful planning. In addition, the accumulation of debris in the higher orbits is not only affected by payload launches into the lower altitudes; collisions in any orbital regime will deposit debris into any other orbital altitudes due to the ΔV imparted during the fragmentation event. Despite the much fewer megaconstellations planned at the higher altitudes, their failure in post-mission disposal or collision avoidance maneuvers will result in a large effect on orbital debris accumulation.

VI. Appendix

A. Variability of B^* in TLEs

A snapshot of the B^* values of the TLEs from January 2023 is shown in this figure. The B^* value is a fitted parameter, and hence the nonphysical negative values for a large number of objects.

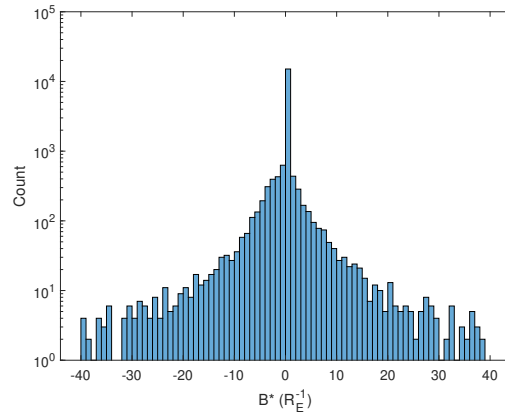


Fig. 31 Distribution B^* values from TLEs (Jan 2023)

B. Resampling for mass and radius of objects

This figure compares the different methods for resampling the physical parameters of missing objects.

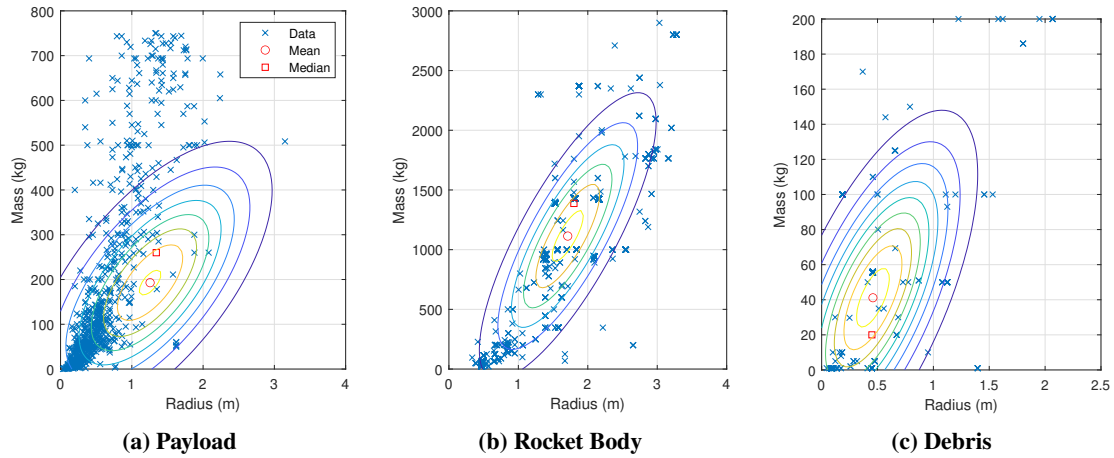


Fig. 32 Parameter resampling for various object classes

C. No Future Launch scenarios

The data used for the *No Future Launches* and *Extrapolated* scenarios with January 2023 epoch are described here. At this epoch, a large portion of the active payloads are from Starlink in the 500 km altitude bin. Table 5 shows the breakdown of each object as described by DISCOS, where MRO represents Mission Related Objects, FD represents Fragmentation Debris, and D represents Debris as defined by ESA [14].

Table 5 Breakdown of object type in the initial population for January 2023

Payload	Payload MRO	Payload Frag. Debris	Payload Debris	Rocket Body
7866	233	5573	95	971
Rocket Body MRO	Rocket Frag. Debris	Rocket Debris	Other Debris	Unknown
609	2808	25	253	1

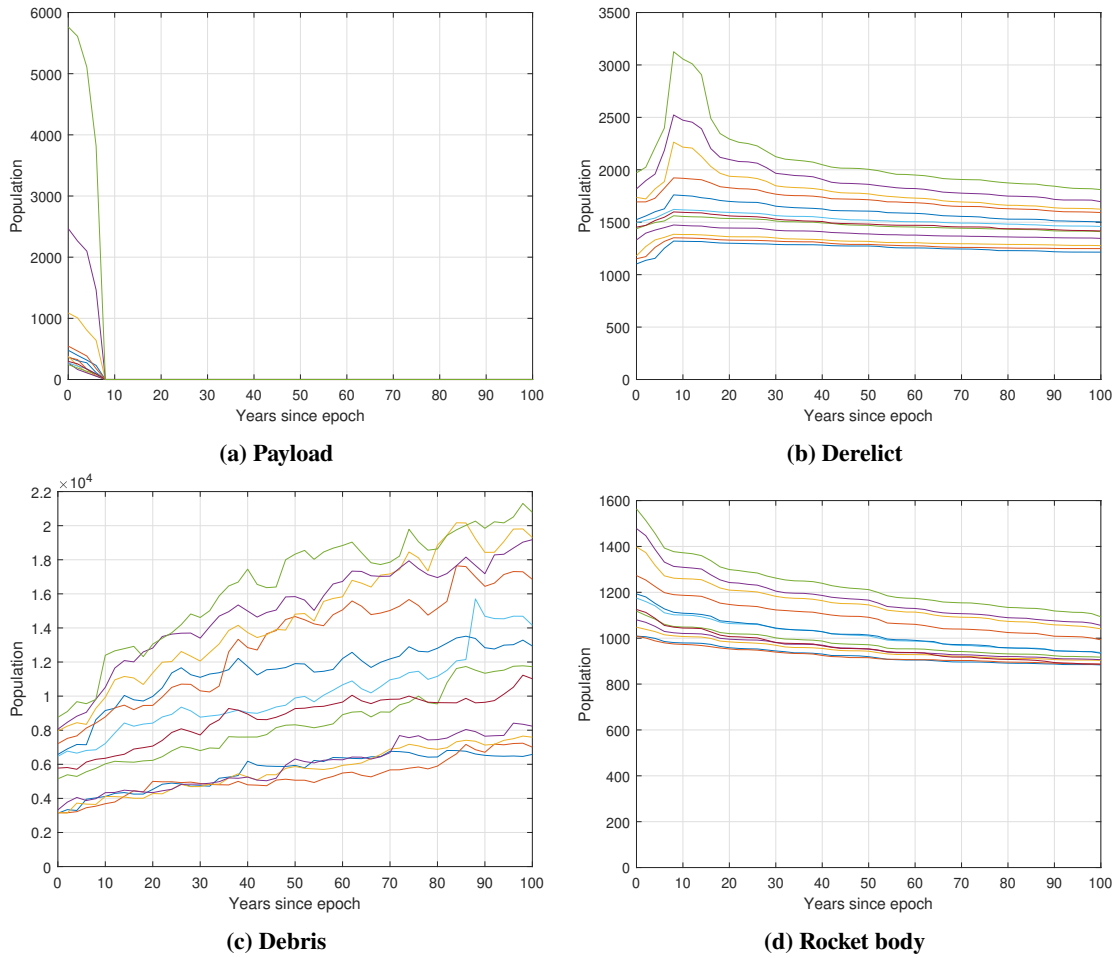


Fig. 33 Number of objects per object type for the No Future Launch cases with varying epochs

D. Megaconstellation future traffic model

Table 6 describes the future megaconstellation modeled in this work compiled from various sources including [96] as of March 2023. *Total num* column denotes the final operational constellation size without spares, *Start Year* and *Finish Year* denotes the start and end of the ramp-up phase to get to the final operational number per constellation. Some constellations are missing some information such as the launch year and physical attributes. Launch dates were estimated for the purposes of the scenarios, and the physical attributes were set equal to the Starlink constellation.

Table 6 Modeled future traffic for megaconstellations

Constellation	Alt (km)	Inc (deg)	Total Num	Start Year	Finish Year	Mass (kg)	Radius (m)
Starlink	550	53	1584	2018	2027	260	2.0
Starlink	570	70	720	2018	2027	260	2.0
Starlink	560	97.6	348	2018	2027	260	2.0
Starlink	540	53.2	1584	2018	2027	260	2.0
Starlink	560	97.6	172	2018	2027	260	2.0
Starlink2A	530	43	2500	2023	2031	800	2.0
Starlink2A	525	53	2500	2023	2031	800	2.0
Starlink2A	535	33	2500	2023	2031	800	2.0
Starlink2	340	53	5280	2023	2031	1250	4.0
Starlink2	345	46	5280	2023	2031	1250	4.0
Starlink2	350	38	5280	2023	2031	1250	4.0
Starlink2	360	96.9	3600	2023	2031	1250	4.0
Starlink2	530	43	860	2023	2031	1250	4.0
Starlink2	525	53	860	2023	2031	1250	4.0
Starlink2	535	33	860	2023	2031	1250	4.0
Starlink2	604	148	144	2023	2031	1250	4.0
Starlink2	614	115.7	324	2023	2031	1250	4.0
OneWeb	1200	87.9	588	2019	2023	150	0.5
OneWeb	1200	55	128	2019	2023	150	0.5
OneWeb	1200	87.9	1764	2025	2028	150	0.5
OneWeb	1200	40	2304	2025	2028	150	0.5
OneWeb	1200	55	2304	2025	2028	150	0.5
Kuiper	590	33	782	2024	2029	700	1.5
Kuiper	590	30	2	2024	2029	700	1.5
Kuiper	610	42	1292	2024	2029	700	1.5
Kuiper	630	51.9	1156	2024	2029	700	1.5

Table 6 Continued: Modeled future traffic for megaconstellations

Constellation	Alt (km)	Inc (deg)	Total Num	Start Year	Finish Year	Mass (kg)	Radius (m)
Guanwang	590	85.0	480	2035	2055	-	-
Guanwang	600	50.0	2000	2035	2055	-	-
Guanwang	508	60.0	3600	2035	2055	-	-
Guanwang	1145	30.0	1728	2035	2055	-	-
Guanwang	1145	40.0	1728	2035	2055	-	-
Guanwang	1145	50.0	1728	2035	2055	-	-
Guanwang	1145	60.0	1728	2035	2055	-	-
Yinhe	511	63.5	1000	-	-	230	0.7
Hanwha	500	97.5	2000	2025	2035	-	-
Lynk	500	97.5	2000	-	-	125	0.5
Astra	700	0	40	-	-	500	-
Astra	690	98.0	504	-	-	500	-
Astra	700	55.0	1792	-	-	500	-
Astra	380	97.0	2240	-	-	500	-
Astra	390	30.0	4896	-	-	500	-
Astra	400	55.0	4148	-	-	500	-
Boeing	1056	54.0	132	2025	2030	-	-
Telesat	1015	99.0	78	2023	-	-	-
Telesat	1325	50.9	220	2023	-	-	-
Telesat	1015	99.0	351	2023	-	-	-
Telesat	1325	50.9	1320	2023	-	-	-
HVNET	1150	55.0	1440	-	-	-	-
SpinLaunch	830	55.0	1190	-	-	150	-
Globalstar3	485	55.0	1260	-	-	-	-
Globalstar3	515	70.0	100	-	-	-	-
Globalstar3	600	55.0	900	-	-	-	-
Globalstar3	620	98.0	100	-	-	-	-
Globalstar3	700	55.0	720	-	-	-	-

Figure 34 shows the unified launch population per time broken into individual constellation planes. The constellation name denotes the altitude in km and inclination in degrees in the parenthesis. Note that *Kuiper (590/30)* includes only two operational satellites.

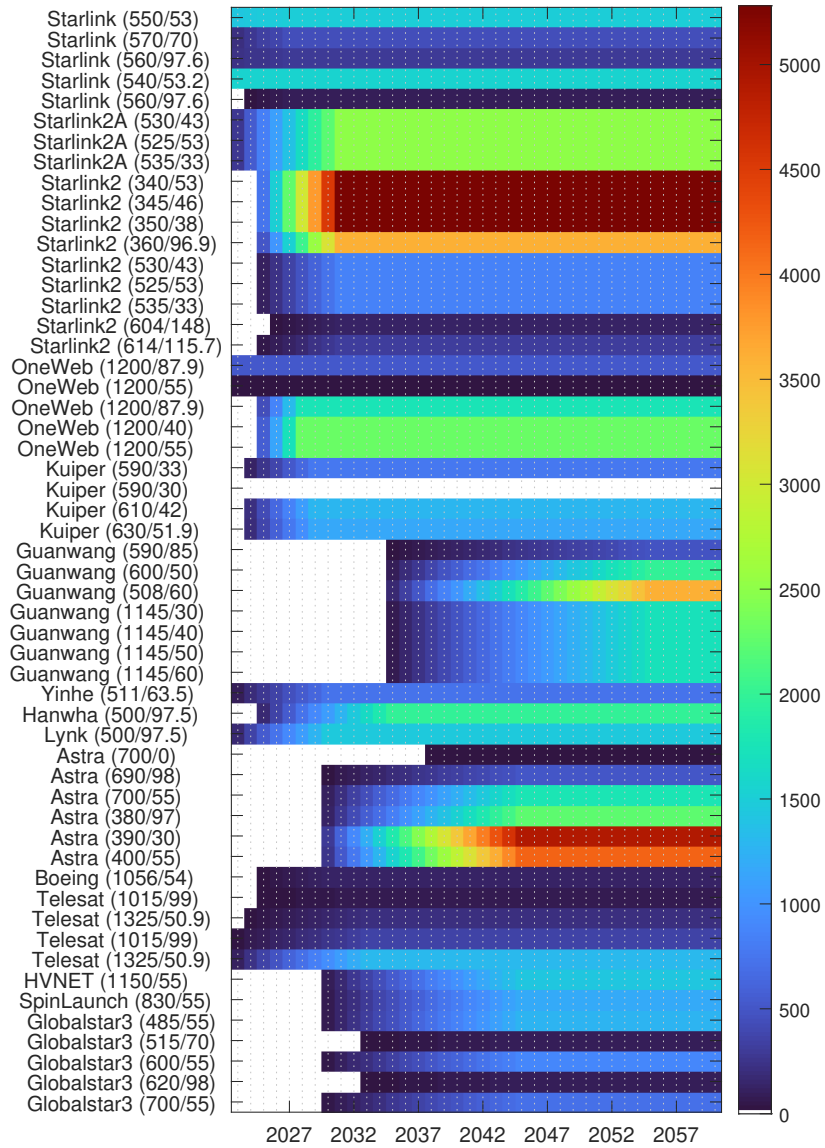


Fig. 34 Megaconstellation population assumption

E. Megaconstellation future traffic model results

Other scenarios that compare portions of megaconstellation launches are shown in this section. Figure 35 shows the evolution of the LEO environment with Starlink, Kuiper, and OneWeb launches, and compares the inclusion and exclusion of Starlink v2, the largest proposed megaconstellation considered in this paper. The plots are binned with an altitude bin of 50 km and a time bin of 1 year.

Figure 36 compares the evolution of megaconstellation launches that are limited to < 600 km (total of 59336 operational megaconstellation payloads) and < 900 km (total of 66598 operational payloads) constellations. The plots are binned with an altitude bin of 50 km and a time bin of 1 year.

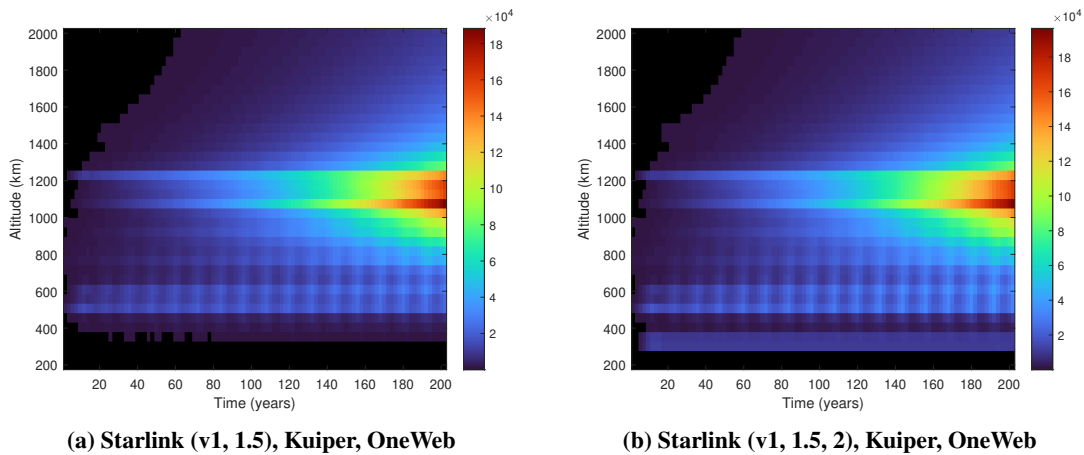


Fig. 35 Total population per altitude for future launches

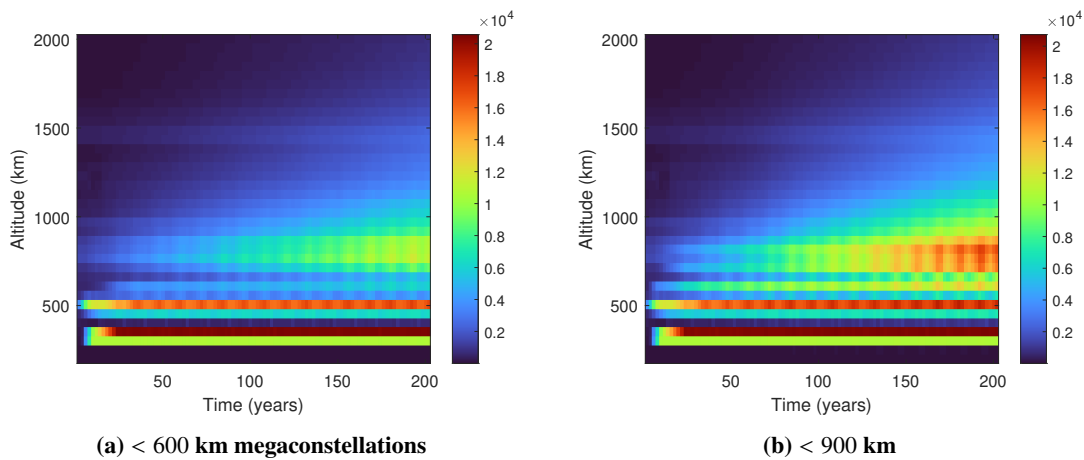


Fig. 36 Population evolution for megaconstellation launches limited to < 600 km and to < 900 km

Acknowledgments

This research was sponsored by MIT Lincoln Scholar Fellowship and the United States Air Force Research Laboratory and the Department of the Air Force Artificial Intelligence Accelerator under Cooperative Agreement Number FA8750-19-2-1000. The views and conclusions contained in this document are those of the authors and should not be interpreted as representing the official policies, either expressed or implied, of the Department of the Air Force or the U.S. Government. The U.S. Government is authorized to reproduce and distribute reprints for Government purposes notwithstanding any copyright notation herein. The authors acknowledge the MIT SuperCloud and Lincoln Laboratory Supercomputing Center for providing the HPC, database, and consultation resources that have contributed to the research results reported within this paper.

References

- [1] SpaceX, “Updates,” 2 2022. URL <https://www.spacex.com/updates/index.html#sustainability>.
- [2] Kessler, D. J., and Cour-Palais, B. G., “Collision Frequency of Artificial Satellites: The Creation of a Debris Belt.” *J Geophys Res*, Vol. 83, 1978, pp. 2637–2646. <https://doi.org/10.1029/JA083iA06p02637>.
- [3] Kessler, D. J., Johnson, N. L., Liou, J.-C., and Matney, M., “The Kessler Syndrome: Implications to Future Space operations,” *33rd Annual Aas Guidance and Control Conference*, 2010.
- [4] Lewis, H. G., Swinerd, G. G., Newland, R. J., and Saunders, A., “The fast debris evolution model,” *Advances in Space Research*, Vol. 44, 2009, pp. 568–578. <https://doi.org/10.1016/j.asr.2009.05.018>.
- [5] Liou, J. C., “An Active Debris Removal Parametric Study for LEO Environment Remediation,” *Advances in Space Research*, Vol. 47, 2011, pp. 1865–1876. <https://doi.org/10.1016/J.ASR.2011.02.003>.
- [6] White, A. E., and Lewis, H. G., “An adaptive strategy for active debris removal,” *Advances in Space Research*, Vol. 53, No. 8, 2014, pp. 1195–1206. <https://doi.org/10.1016/j.asr.2014.01.021>.
- [7] Hakima, H., and Emami, M. R., “Assessment of active methods for removal of LEO debris,” *Acta Astronautica*, Vol. 144, 2018, pp. 225–243. <https://doi.org/10.1016/j.actaastro.2017.12.036>.
- [8] Servadio, S., Simha, N., Gusmini, D., Jang, D., St. Francis, T., D’Ambrosio, A., Lavezzi, G., and Linares, R., “Risk Index for the Optimal Ranking of Active Debris Removal Targets,” *Journal of Spacecraft and Rockets*, Vol. 0, No. 0, 0, pp. 1–14. <https://doi.org/10.2514/1.A35752>.
- [9] “Space Innovation: Mitigation of Orbital Debris in the New Space Age [Press Release],” 9 2022. URL www.fcc.gov.
- [10] Johnson, C. D., “Handbook For New Actors In Space,” 2017.
- [11] Space Safety Coalition, “Best Practices for the Sustainability of Space Operations,” 9 2019.

- [12] SpaceX, OneWeb, and Iridium, “Satellite Orbital Safety Best Practices,” 9 2022.
- [13] Executive Office of the President, “National Space Traffic Management Policy,” *Presidential Document*, Vol. 2018-13521, 2018, pp. 28969–28976. URL <https://www.federalregister.gov/documents/2018/06/21/2018-13521/national-space-traffic-management-policy>.
- [14] ESA Space Debris Office, “ESA Annual Space Environment Report,” 4 2022.
- [15] Colvin, T. J., Karcz, J., and Wusk, G., “Cost and benefit analysis of orbital debris remediation,” *NASA Office of Technology, Policy, and Strategy*, 2023. URL <https://ntrs.nasa.gov/citations/20230002817>.
- [16] FCC, “Space Innovation IB Docket No. 22-271 Mitigation of Orbital Debris in the New Space Age,” Docket No: 22-271, 18-313, 12 2022. URL https://docs.fcc.gov/public/attachments/FCC-22-74A1_Rcd.pdf.
- [17] United Nations, “Destructive direct-ascent anti-satellite missile testing : resolution / adopted by the General Assembly,” 12 2022. URL <https://digitallibrary.un.org/record/3996915>.
- [18] “Space Industry Statement in Support of International Commitments Not To Conduct Destructive Anti-Satellite Testing,” 3 2024. URL https://swfound.org/media/207814/da-asat-statement_march-2024.pdf.
- [19] Letizia, F., Colombo, C., Lewis, H., and Krag, H., “Extending the ECOB space debris index with fragmentation risk estimation,” *European Space Agency (ESA)*, 2017.
- [20] Krag, H., Lemmens, S., and Letizia, F., “Space traffic management through the control of the space environment’s capacity,” *5th European Workshop on Space Debris Modeling and Remediation*, 2018.
- [21] Rossi, A., Valsecchi, G. B., and Alessi, E. M., “The Criticality of Spacecraft Index,” *Advances in Space Research*, Vol. 56, 2015, pp. 449–460. <https://doi.org/10.1016/J.ASR.2015.02.027>.
- [22] McKnight, D., Witner, R., Letizia, F., Lemmens, S., Anselmo, L., Pardini, C., Rossi, A., Kunstadter, C., Kawamoto, S., Aslanov, V., Perez, J. C. D., Ruch, V., Lewis, H., Nicolls, M., Jing, L., Dan, S., Dongfang, W., Baranov, A., and Grishko, D., “Identifying the 50 statistically-most-concerning derelict objects in LEO,” *Acta Astronautica*, Vol. 181, 2021, pp. 282–291. <https://doi.org/10.1016/j.actaastro.2021.01.021>.
- [23] Volterra, V., “Fluctuations in the abundance of a species considered mathematically,” *Nature*, Vol. 118, No. 2972, 1926, pp. 558–560.
- [24] Lotka, A. J., “Analytical note on certain rhythmic relations in organic systems,” *Proceedings of the National Academy of Sciences*, Vol. 6, No. 7, 1920, pp. 410–415.
- [25] Talent, D., “Analytical model for orbital debris environmental management,” 1990. URL <https://ntrs.nasa.gov/citations/19900045002>.
- [26] JASON report, “The Impacts of Large Constellations of Satellites,” 2020.

- [27] Lifson, M., Jang, D., Pasiecznik, C., and Linares, R., “MOCAT-SSEM: A Source-Sink Evolutionary Model for Space Debris Environment Evolutionary Modeling,” *9th Annual Space Traffic Management Conference*, 2023.
- [28] Gusmini, D., D’Ambrosio, A., Servadio, S., Siew, P. M., Di Lizia, P., and Linares, R., “Effects of Orbit Raising and Deorbiting in Source-Sink Evolutionary Models,” *Journal of Spacecraft and Rockets*, Vol. 0, No. 0, 0, pp. 1–14. <https://doi.org/10.2514/1.A35849>.
- [29] D’Ambrosio, A., Servadio, S., Mun Siew, P., and Linares, R., “Novel Source–Sink Model for Space Environment Evolution with Orbit Capacity Assessment,” *Journal of Spacecraft and Rockets*, Vol. 60, No. 4, 2023, pp. 1112–1126. <https://doi.org/10.2514/1.A35579>.
- [30] D’Ambrosio, A., and Linares, R., “Carrying Capacity of Low Earth Orbit Computed Using Source-Sink Models,” *Journal of Spacecraft and Rockets*, 2024, pp. 1–17. <https://doi.org/10.2514/1.A35729>.
- [31] Liou, J. C., Hall, D. T., Krisko, P. H., and Opiela, J. N., “LEGEND – a Three-dimensional LEO-to-GEO Debris Evolutionary Model,” *Advances in Space Research*, Vol. 34, 2004, pp. 981–986. <https://doi.org/10.1016/J.ASR.2003.02.027>.
- [32] Lewis, H., Swinerd, G., Williams, N., and Gittins, G., “DAMAGE: a Dedicated GEO Debris Model Framework,” *3rd European Conference on Space Debris*, 2001, pp. 373–378.
- [33] Lewis, H. G., Saunders, A., Swinerd, G., and Newland, R. J., “Effect of thermospheric contraction on remediation of the near-Earth space debris environment,” *Journal of Geophysical Research: Space Physics*, Vol. 116, 2011. <https://doi.org/10.1029/2011JA016482>.
- [34] Dolado-perez, J., Di Costanzo, R., and Revelin, B., “Introducing Medee-a New Orbital Debris Evolutionary Model,” Darmstadt, Germany, 2013, pp. 22–25.
- [35] Martin, C. E., Cheese, J. E., and Klinkrad, H., “Space Debris Environment Analysis with DELTA 2.0,” *International Astronautical Federation - 55th International Astronautical Congress 2004*, 2004. <https://doi.org/10.2514/6.IAC-04-IAA.5.12.5.04>.
- [36] Radtke, J., Mueller, S., Schaus, V., and Stoll, E., “LUCA2 - An enhanced long-term utility for collision analysis | ESA Proceedings Database,” 2017.
- [37] Sorge, M. E., and Mains, D. L., “IMPACT Fragmentation Model Improvements,” *AIAA/AAS Astrodynamics Specialist Conference*, 2014. <https://doi.org/10.2514/6.2014-4228>.
- [38] Wang, X. W., and Liu, J., “An Introduction to a New Space Debris Evolution Model: SOLEM,” *Advances in Astronomy*, Vol. 2019, 2019. <https://doi.org/10.1155/2019/2738276>.
- [39] Drmola, J., and Hubik, T., “Kessler Syndrome: System Dynamics Model,” *Space Policy*, Vol. 44-45, 2018, pp. 29–39. <https://doi.org/10.1016/J.SPACEPOL.2018.03.003>.
- [40] Rosengren, A. J., Skoulidou, D. K., Tsiganis, K., and Voyatzis, G., “Dynamical cartography of Earth satellite orbits,” *Advances in Space Research*, Vol. 63, 2019, pp. 443–460. <https://doi.org/10.1016/J.ASR.2018.09.004>.

- [41] Giudici, L., Colombo, C., Horstmann, A., Letizia, F., and Lemmens, S., “Density-based evolutionary model of the space debris environment in low-Earth orbit,” *Acta Astronautica*, Vol. 219, 2024, pp. 115–127. <https://doi.org/10.1016/j.actaastro.2024.03.008>.
- [42] Johnson, N. L., Krisko, P. H., Liou, J. C., and Anz-Meador, P. D., “NASA’s New Breakup Model of EVOLVE 4.0,” *Advances in Space Research*, Vol. 28, 2001, pp. 1377–1384. [https://doi.org/10.1016/S0273-1177\(01\)00423-9](https://doi.org/10.1016/S0273-1177(01)00423-9).
- [43] Liou, J. C., Kessler, D. J., Matney, M., and Stansbery, G., “A New Approach To Evaluate Collision Probabilities Among Asteroids, Comets, And Kuiper Belt Objects,” *Lunar and Planetary Science XXXIV*, 2003.
- [44] Liou, J. C., “Collision activities in the future orbital debris environment,” *Advances in Space Research*, Vol. 38, 2006, pp. 2102–2106. <https://doi.org/10.1016/j.asr.2005.06.021>.
- [45] MIT ARCLab, “MOCAT-MC GitHub Repository,” <https://github.com/ARCLab-MIT/MOCAT-MC>, 2024.
- [46] Vallado, D., Crawford, P., Hujsak, R., and Kelso, T., “Revisiting Spacetrack Report #3,” *AIAA/AAS Astrodynamics Specialist Conference and Exhibit*, 2006. <https://doi.org/10.2514/6.2006-6753>.
- [47] Martinusi, V., Dell’Elce, L., and Kerschen, G., “Analytic propagation of near-circular satellite orbits in the atmosphere of an oblate planet,” *Celestial Mechanics and Dynamical Astronomy*, Vol. 123, 2015, pp. 85–103. <https://doi.org/10.1007/s10569-015-9630-7>.
- [48] Cefola, P., Folcik, Z., Di-Costanzo, R., Bernard, N., Setty, S., and Juan, J., “Revisiting the DSST standalone orbit propagator,” *Advances in the Astronautical Sciences*, Vol. 152, 2014, pp. 2891–2914.
- [49] Vallado, D. A., *Fundamentals of Astrodynamics and Applications*, 5th ed., Microcosm Press, 2022.
- [50] Horstmann, A., Hesselbach, S., Wiedemann, C., Flegel, S., Oswald, M., and Krag, H., “Enhancement of S/C Fragmentation and Environment Evolution Models,” *European Space Agency*, 2020.
- [51] Bowman, B., Tobiska, W. K., Marcos, F., Huang, C., Lin, C., and Burke, W., “A new empirical thermospheric density model JB2008 using new solar and geomagnetic indices,” 2008, p. 6438.
- [52] Tobiska, W. K., Bowman, B., and Bouwer, S. D., “Solar and geomagnetic indices for the JB2008 thermosphere density model,” *Contract*, Vol. 19628, No. 03-C, 2008, p. 0076.
- [53] Hoots, F. R., and Roehrich, R. L., “Spacetrack Report No. 3: Models for propagation of NORAD element sets,” Tech. rep., Aerospace Defense Center, Peterson Air Force Base, 1980.
- [54] Acedo, L., “Kinematics effects of atmospheric friction in spacecraft flybys,” , 2017.
- [55] Lewis, H. G., Diserens, S., Maclay, T., and Sheehan, J. P., “Limitations of the cube method for assessing large constellations,” *First International Orbital Debris Conference*, 2019.

- [56] Alarcón Rodríguez, J. R., Martínez Fadrique, F., and Klinkrad, H., “Collision Risk Assessment with a ‘Smart Sieve’ Method,” 2002, p. 159.
- [57] George, E. R., “A High Performance Conjunction Analysis Technique for Cluster and Multi-Core Computers,” *AMOS*, 2011.
- [58] Lue, A., “The All-Versus-All Low Earth Orbit Conjunction Problem,” *AMOS*, 2011.
- [59] Klinkrad, H., *Space Debris: Models and Risk Analysis*, Springer Berlin Heidelberg, 2006.
- [60] Frey, S., and Colombo, C., “Transformation of satellite breakup distribution for probabilistic orbital collision hazard analysis,” *Journal of Guidance, Control, and Dynamics*, Vol. 44, 2021, pp. 88–105. <https://doi.org/10.2514/1.G004939>.
- [61] Finkleman, D., Oltrogge, D. L., Faulds, A., and Gerber, J., “Analysis of the response of a space surveillance network to orbital debris events,” American Astronautical Society, San Diego, CA, 2008.
- [62] Heard, W. B., “Dispersion of ensembles of non-interacting particles,” *Astrophysics and Space Science*, Vol. 43, No. 1, 1976, pp. 63–82. <https://doi.org/10.1007/BF00640556>.
- [63] Cordelli, A., “The Proliferation of Orbiting Fragments: A Simple Mathematical Model,” *Science & Global Security*, Vol. 2, No. 4, 1991, pp. 365–378. <https://doi.org/10.1080/08929889108426373>.
- [64] Frazzoli, E., Palmerini, G. B., and Graziani, F., “Debris cloud evolution: Mathematical modelling and application to satellite constellation design,” *Acta Astronautica*, Vol. 39, No. 6, 1996, pp. 439–445. [https://doi.org/10.1016/S0094-5765\(96\)00156-7](https://doi.org/10.1016/S0094-5765(96)00156-7).
- [65] Rossi, A., Lewis, H., White, A., Anselmo, L., Pardini, C., Krag, H., and Bastida Virgili, B., “Analysis of the consequences of fragmentations in low and geostationary orbits,” *Advances in Space Research*, Vol. 57, No. 8, 2016, pp. 1652–1663. <https://doi.org/10.1016/J.ASR.2015.05.035>.
- [66] Lewis, H. G., Radtke, J., Rossi, A., Beck, J., Oswald, M., Anderson, P., Bastida Virgili, B., and Krag, H., “Sensitivity of the Space Debris Environment to Large Constellations and Small Satellites,” *Journal of the British Interplanetary Society*, Vol. 70, 2017, pp. 105–117.
- [67] Letizia, F., “Extension of the density approach for debris cloud propagation,” *Journal of Guidance, Control, and Dynamics*, Vol. 41, No. 12, 2018, pp. 2650–2656. <https://doi.org/10.2514/1.G003675>.
- [68] Su, S. Y., and Kessler, D. J., “Contribution of explosion and future collision fragments to the orbital debris environment,” *Advances in Space Research*, Vol. 5, No. 2, 1985, pp. 25–34. [https://doi.org/10.1016/0273-1177\(85\)90384-9](https://doi.org/10.1016/0273-1177(85)90384-9).
- [69] Ruch, V., Serra, R., Omary, P., and Dolado Perez, J. C., “Decoupled Analysis of the Effect of Past and Future Space Activity on the Orbital Environment,” *8th European Conference on Space Debris*, 2021, pp. 20–23.
- [70] Dell’Elce, L., Arnst, M., and Kerschen, G., “Probabilistic assessment of the lifetime of low-earth-orbit spacecraft: Uncertainty characterization,” *Journal of Guidance, Control, and Dynamics*, Vol. 38, No. 5, 2015, pp. 900–912. <https://doi.org/10.2514/1.G000148>.

- [71] Luo, Y. z., and Yang, Z., “A review of uncertainty propagation in orbital mechanics,” *Progress in Aerospace Sciences*, Vol. 89, 2017, pp. 23–39. <https://doi.org/10.1016/J.PAEROSCI.2016.12.002>.
- [72] Lewis, H. G., “Understanding long-term orbital debris population dynamics,” *First Int’l. Orbital Debris Conf.*, 2019.
- [73] Weeden, B., “Anti-satellite Tests in Space— The Case of China,” 2013. URL https://swfound.org/media/115643/china_asat_testing_fact_sheet_aug_2013.pdf.
- [74] Kelso, T. S., “Analysis of the Iridium 33-Cosmos 2251 Collision,” 2009. URL <http://celestrak.com/SOCRATES/>.
- [75] Stansbery, G., Matney, M., Liou, J. C., and Whitlock, D., “A Comparison of Catastrophic On-Orbit Collisions,” 2008.
- [76] Braun, V., Lemmens, S., Reihls, B., Krag, H., and Horstmann, A., “Analysis of Breakup Events,” 2017.
- [77] Servadio, S., Jang, D., and Linares, R., “Threat Level Estimation From Possible Break-Up Events In LEO,” 2024, p. 1065.
- [78] Weeden, B., “2009 Iridium-Cosmos Collision Fact Sheet,” , 2010. URL https://swfound.org/media/6575/swf_iridium_cosmos_collision_fact_sheet_updated_2012.pdf.
- [79] Pultarova, T., “SpaceX Starlink satellites had to make 25,000 collision-avoidance maneuvers in just 6 months — and it will only get worse,” <https://www.space.com/starlink-satellite-conjunction-increase-threatens-space-sustainability>, 2023. Accessed: 2023-07-07.
- [80] Moomey, L. C. D., Falcon, R., and Khan, A., “Trending and analysis of payload vs. All low earth conjunction data messages below 1000 km, from 2016 through 2021,” *Journal of Space Safety Engineering*, Vol. 10, No. 2, 2023, pp. 217–230. <https://doi.org/10.1016/j.jsse.2023.03.006>.
- [81] Liou, J., Anilkumar, A., Virgili, B. B., Hanada, T., Krag, H., Lewis, H., Raj, M., Rao, M., Rossi, A., and Sharma, R., “Stability of the Future LEO Environment - an IADC Comparison Study,” *Proc. 6th European Conference on Space Debris*, 2013.
- [82] Reuther, A., Kepner, J., Byun, C., Samsi, S., Arcand, W., Bestor, D., Bergeron, B., Gadepally, V., Houle, M., Hubbell, M., Jones, M., Klein, A., Milechin, L., Mullen, J., Prout, A., Rosa, A., Yee, C., and Michaleas, P., “Interactive Supercomputing on 40,000 Cores for Machine Learning and Data Analysis,” *2018 IEEE High Performance Extreme Computing Conference, HPEC 2018*, 2018. <https://doi.org/10.1109/HPEC.2018.8547629>.
- [83] Liou, J.-C., “Orbital Debris Modeling and the Future Orbital Debris Environment,” *Orbital Debris Lecture (ASEN 6519)*, 2012.
- [84] Liou, J.-C., and Johnson, N., “A LEO satellite postmission disposal study using LEGEND,” *Acta Astronautica*, Vol. 57, 2005, pp. 324–329. <https://doi.org/10.1016/j.actaastro.2005.03.002>.
- [85] Liou, J. C., Johnson, N. L., and Hill, N. M., “Controlling the growth of future LEO debris populations with active debris removal,” *Acta Astronautica*, Vol. 66, No. 5-6, 2010, pp. 648–653. <https://doi.org/10.1016/J.ACTAASTRO.2009.08.005>.
- [86] Liou, J.-C., and Krisko, P., “An Update on the Effectiveness of Postmission Disposal in LEO,” *64th International Astronautical Congress (IAC)*, 2013.

- [87] Lewis, H. G., Swinerd, G. G., Newland, R. J., and Saunders, A., “Active Removal Study for On-Orbit Debris Using DAMAGE,” *5th European Conference on Space Debris*, 2009.
- [88] Lewis, H. G., and Marsh, N., “Deep Time Analysis of Space Debris and Space Sustainability,” 2021, p. 153.
- [89] White, A. E., and Lewis, H. G., “The many futures of active debris removal,” *Acta Astronautica*, Vol. 95, No. 1, 2014, pp. 189–197. <https://doi.org/10.1016/j.actaastro.2013.11.009>.
- [90] Virgili, B. B., “DELTA (Debris Environment Long-Term Analysis),” *6th International Conference on Astrodynamics Tools and Techniques (ICATT)*, 2016.
- [91] ESA Space Debris Office, “ESA Annual Space Environment Report,” 9 2023.
- [92] Letizia, F., Bella, D., Weber, D., Bastida Virgili, B., Lemmens, S., and Soares, T., “Long-term Environment Simulations and Risk Characterization in Support of a Zero Debris Policy,” *2nd International Orbital Debris Conference*, LPI Contributions, Vol. 2852, 2023, p. 6029.
- [93] Bastida Virgili, B., Dolado, J., Lewis, H., Radtke, J., Krag, H., Revelin, B., Cazaux, C., Colombo, C., Crowther, R., and Metz, M., “Risk to space sustainability from large constellations of satellites,” *Acta Astronautica*, Vol. 126, 2016, pp. 154–162. <https://doi.org/10.1016/j.actaastro.2016.03.034>, space Flight Safety.
- [94] D’Ambrosio, A., Servadio, S., Siew, P. M., Jang, D., Lifson, M., and Linares, R., “Analysis Of The Leo Orbital Capacity Via Probabilistic Evolutionary Model,” 2022.
- [95] Jang, D., D’Ambrosio, A., Lifson, M., Pasiecznik, C., and Linares, R., “Stability of the LEO Environment as a Dynamical System,” 2022.
- [96] McDowell, J., *Jonathan’s Space Report*, Jonathan McDowell, 2023.
- [97] Henry, C., “SpaceX submits paperwork for 30,000 more Starlink satellites,” *Space News*, Vol. 15, 2019, p. 2019.
- [98] Diaz, P., Mesalles Ripoll, P., Duncan, M., Lindsay, M., Harris, T., and Lewis, H. G., “Data-Driven Lifetime Risk Assessment and Mitigation Planning for Large-Scale Satellite Constellations,” *The Journal of the Astronautical Sciences*, Vol. 70, No. 4, 2023, p. 21.